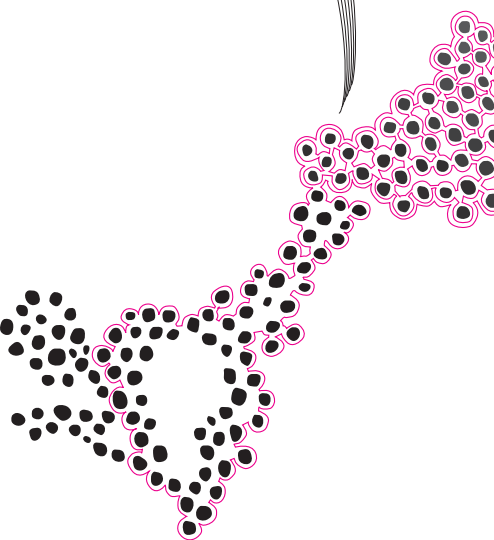MSc Thesis Applied Mathematics
and Applied Physics

Impact of Hybridization on Edge States in SnTe

William Schaarman

Supervisors:
Alexander Brinkman
Bernard Geurts
Maarten Kamphuis

11th December 2024

Department of Applied Mathematics
Faculty of Electrical Engineering,
Mathematics and Computer Science

Department of Applied Physics
Faculty of Science and Technology

UNIVERSITY OF TWENTE.

Contents

1 Introduction

Topological insulators (TIs) have been studied in recent years for various applications. For example, they are considered a basis for quantum computing as the Majorana modes they can theoretically host can provide a robust environment for qubits, even under disorder [1, 2]. Their special properties come from the the modes they can host, which are surface states that are protected by time-reversal symmetry. In the last decade, more materials have been discovered that also host these surface states but instead are additionally protected by crystal symmetries. These materials are topological crystalline insulators (TCIs) [3].

In 2012 Hsieh et al. published a study on the theoretical properties of tin telluride (SnTe) and lead telluride (PbTe) [4]. In this work, the claim was made that SnTe belongs to the group of topological crystalline insulators. TCIs are a special subgroup of topological insulators [5]. TIs have the special property of containing conducting channels only on the material's surface while the bulk is insulating. The consequence of this is a linear crossing called a Dirac cone in the band structure. These states are called surface states and they only exist if specific symmetries, which are inherent to the material, remain.

In 2017 Schindler et al. [6] described higher-order topological insulator (HOTI) states with SnTe as an example. In this paper, they broke the symmetry that protects the surface states while keeping the symmetry that protects the edge states. This implies we go from a 3D structure to a 1D channel, which is a HOTI. The main advantage of these HOTI states is that they will be fully 1D in contrast to the more common surface states which are 2D. If we have a 1D channel then, due to spin momentum locking, backscattering will not occur as the electron would have to both switch momentum and switch spin to travel in the opposite direction, which is forbidden since the spin states are orthogonal.

These 1D HOTI states are in two ways, especially valuable. It is theorized that by combining strong topological insulators and an s-wave superconductor into an STIs structure, Majorana bound states (MBS) can be created at the interface between the TI and superconductor [7]. While this also holds for a 2D system, a 1D system would have the advantage of the MBS being more localized compared to the 2D case, which can make it easier to measure the state. MBS can then be used for the creation of qubits, one of the fundamental components of the quantum computer. Secondly, as mentioned before, due to the absence of backscattering, there will be zero resistance without it being in a superconducting state. This becomes useful as this would allow a wire with little energy dissipation as there cannot be any scattering, which would increase the efficiency of electronic transport.

While a lot is already known about the HOTI states, the effects of hybridization on these edge channels have to be investigated. This is the effect where two wave functions on opposite surfaces interact, changing the band structure of the material. In Bismuth signs of HOTI states have already been shown [8]. Hence this thesis will seek to create a better understanding of SnTe and its properties as a TCI under hybridization. This will be accomplished using two models. One model is an analytical low-energy approximation of the Hamiltonian and will describe the most important features that give rise to the surface states. The second one is a numerical tight-binding simulation of the material where the orbitals of the atoms are modeled together with the interactions they have with each other. This approach is used to more accurately determine which physical mechanisms can be exploited to achieve these states experimentally. This gives the general goal of analyzing the energy gap found due to hybridization and checking the robustness of the HOTI states in this gap.

We find that the edge states in SnTe are robust against hybridization, even when considering wires that hybridize in multiple directions. This is shown through an examination of the wave density for a semi-infinite tight-binding model. We also find that the odd and even termination of SnTe for small wires still plays a large effect on the bandgap. This effect is rather large as the penetration depth is estimated to be in the order of 10 nm.

The organization of this thesis is as follows. In Section 2 we discuss the theoretical foundation of the TI and TCI. Section 3 is devoted to a discussion of the low-energy model employed here. Key results regarding the tight-binding approach are presented in section 4 and concluding remarks are made in section 5. Finally, a Discussion of the results is presented in section 6 followed by an outlook in section 7.

2 A review of TCIs and their properties

In this section, we will discuss the background on how topological insulators work and the hybridization of the surface states, in section 2.1.1 and 2.1.2 respectively. Then we will discuss the implications of the crystal symmetries of SnTe in section 2.2.1. Followed by a dissection of the particular surface states for SnTe in 2.2.2. Finally, there will be some additional considerations for SnTe regarding the edge states it can host in 2.2.3.

2.1 Physics of a TI

Generally, a topological insulator (TI) can be described as a material with conducting modes restricted to parts of the material that have a lower dimension. For a three-dimensional TI, this manifests as conducting surface states in the material while the bulk of the material acts as an insulator. These lower-dimensional conducting modes arise from and are protected by symmetry constraints on the Hamiltonian. But before we have a detailed look at the implications of this, we will first have a brief look at the field of topology in general.

2.1.1 A glance at a TI

To introduce topological insulators, we can first look at the field of topology. Topology is the branch of mathematics that studies properties of spaces that are invariant under continuous deformation [9]. A well-known example is the comparison of the doughnut and the coffee cup. For a 3D object, we can see that a hole cannot be added or removed with continuous transformations [10]. Hence we can call the number of holes a topological invariant of an object under these conditions. If we consider a coffee cup and a doughnut under this lens, we can see that these objects are in the same similarity class as they both have one hole, while for example, a bowl has no holes and hence would fall into a different topological class.

For topological insulators, a picture is generally sketched of two materials next to each other. One material is a regular insulator while the other is a topological insulator. The insulator has a large band gap and the TI has one too, however, for the TI this band gap is inverted as given in Fig. 1, indicated by the different colors. As the band gap is inverted compared to the insulator, a transition will occur when you go from one material to the other. Along this transition, the band gap must close as the transition is continuous and the character of the bands switched. This transition will hence have to occur at the interface between these two materials, or in other words, the surface of the TI. This transition creates a crossing which must always be present as long as the bandgap is inverted.

Now a bit more detail about the topological invariant. In our case, this is the Chern number which describes the topology. In general, when we have a nonzero Chern number for a material, it is in a topological regime while a Chern number of zero describes a trivial insulator. This number, just like what we previously defined as 'having a hole or not' can only attain certain values which depend on the symmetries involved. It also cannot be changed unless some transformation breaks the system's symmetries that protect the topology. For a general topological insulator, the symmetry to break is often T-symmetry but we can also consider others as will be explained.

Now one could ask, how do we define a topological invariant to classify these phases? To this end, we look at the symmetries present in the material [12]. In any system, we have three main symmetries which dictate the behavior of the topological invariant.
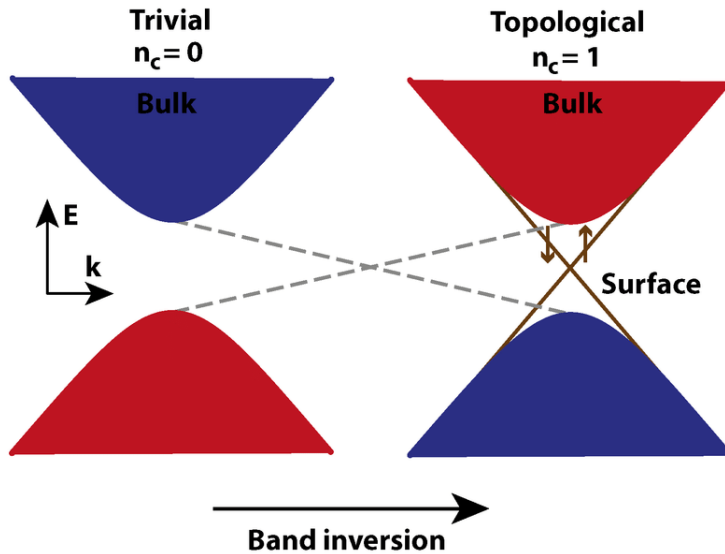
FIGURE 1: **Band inversion**
An overview of the argument of how surface states on a TI arise. If we go from the trivial side to the topological side we see that the gap (dashed line) must close to invert the bands. n_c indicates the value of the topological invariant. $n_c = 1$ implies a topological bandgap while $n_c = 0$ implies a trivial bandgap [11].

These symmetries are time-reversal symmetry (T), particle-hole symmetry (P), and chiral symmetry (C). Together these form the main topological classes defined by the presence or absence of these symmetries [13]. While they are all relevant for general cases, for now, our concern lies with time-reversal symmetry, as this is one of the relevant symmetries in the systems we look at.

If we only consider T-symmetry, we have Kramer pairs by Kramers' degeneracy theorem [14]. This states that for every eigenstate of a system with T-symmetry with half-integer spin, we have another eigenstate with the same energy and opposite spin which is related due to T-symmetry. This is a pair of degenerate conducting modes described by $T|\Psi_{\uparrow,k}\rangle = |\Psi_{\downarrow,-k}\rangle$. Due to this degeneracy, the number of crossings in a band structure can only change by two at a time. Often, when there are two crossings in a band structure, this will result in a trivial system as the topological invariant switches with each crossing. This is the result of many topological invariants belonging to the $\mathbb{Z}_2$ class.

If we have time-reversal symmetry in the system, then the crossings can only happen at certain points in the Brillouin zone. These are the time-reversal invariant momenta (TRIM). The location of the TRIMs can be found by considering that for Kramer pairs we have $T|\Psi_{\uparrow,0}\rangle = |\Psi_{\downarrow,0}\rangle$ or $T|\Psi_{\uparrow,\pi}\rangle = |\Psi_{\downarrow,\pi}\rangle$. As the Brillouin zone has a periodicity of 2π we find that when the gap closes at either of these points in the band structure, this will result in a single crossing for the bands. This will result in the topological invariant changing by one and will hence put the material in a topological state.

These bands, which cross the energy gap, form the shape of a cone, which is called the Dirac cone. The point where the linear bands cross each other is referred to as the Dirac point. A sketch of both can be seen in Fig. 2. If we consider the wave functions which correspond to the energies in the Dirac cone we would find that these are localized at the surface.
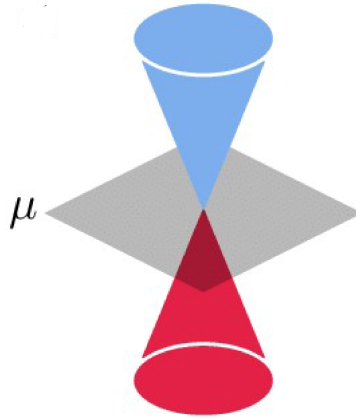

FIGURE 2: **Dirac cone**
A graphical presentation of a Dirac cone. This is a linear dispersion relation in k-space. In this case, k-space is projected to be 2-dimensional giving a cone shape for the Dirac cone. μ is the energy level exactly at the closing of the Dirac cone. Adapted from: [15]

2.1.2 Hybridization of surface states

First, we touch on the phenomenon called hybridization of the surface states, which refers to two opposite surface states interacting when they are close in proximity to each other. While the wave functions of a surface state are localized at the surface of a material, they decay exponentially into the bulk. This causes the two wave functions to overlap which implies that two wave functions will interact. As the surface states get close to each other the overlap increases and hence the interaction between the two surface states increases. This interaction changes the energy levels as the degeneracy of the overlapping tails is lifted by opening up a hybridization gap [16]. The effects of hybridization typically only happen at a nanometer scale, otherwise, the overlap of the wave function is too small to have a noticeable effect. Still, the effect becomes significant in thin films and nanowires.

2.2 SnTe

In 2012, Hsieh et al.theoretically predicted SnTe to be a TCI [4]. This was later confirmed experimentally by angle-resolved photoemission spectroscopy [17]. This special variant of a TI has additional symmetry constraints imposed by the crystal structure that protect its topological states. When these spatial symmetries or time-reversal symmetry are broken, a phase transition to the trivial state would occur. Because of the spacial symmetries it needs SnTe belongs to the class of topological crystalline insulators (TCI)

2.2.1 Symmetries

SnTe forms in a rock-salt crystal, as can be seen in Fig. 3. This structure belongs to the symmetry group C_4 which can be described by the following basis: A rotation of $\frac{2\pi}{3}$ around the [111] axis, a reflection concerning the (110) plane and inversion symmetry.
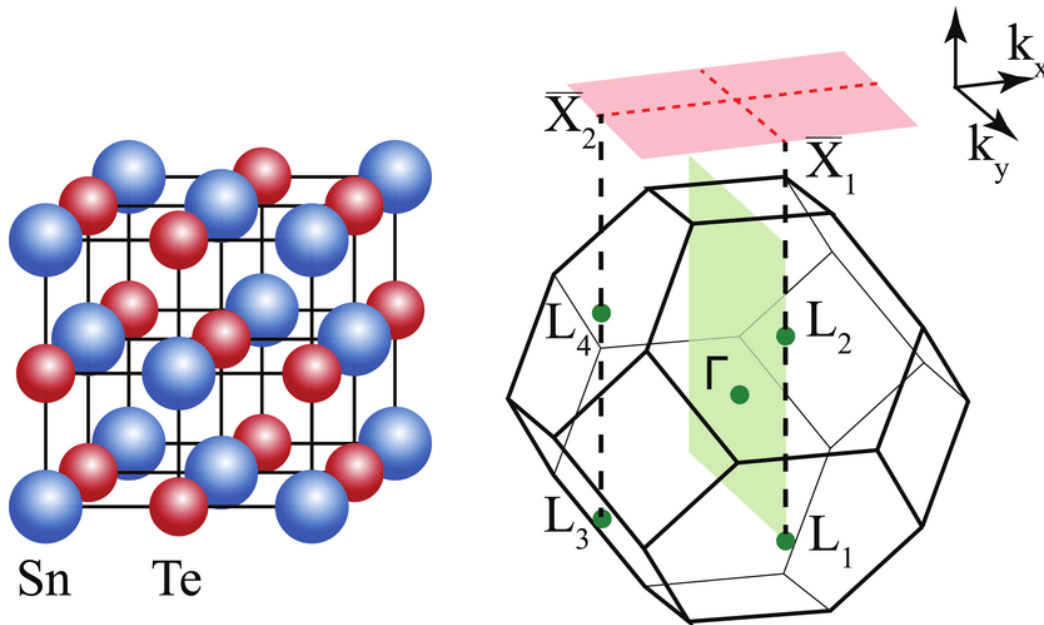

FIGURE 3: **Lattice and 3D Brillouin zone of SnTe**
On the left the crystal structure of SnTe is given. Here one can see the three symmetries. If one takes the origin at any atom one can rotate around the [111] axis a total of 3 times. Also, there is a mirror symmetry compared to the (110) plane. Lastly, inversion symmetry holds at any site in the crystal. On the right, the Brillouin zone is given with a projection to the (001) plane.
Adapted from: [18].

Just like a regular TI SnTe has a topological invariant as it has a protected topological state. However, if we would determine the Chern number of SnTe we will see that this is zero, which implies that our material should not have surface states. Instead of the Chern number, the mirror Chern number is the topological invariant for SnTe. This invariant specifically exists because of the different symmetries found in SnTe.

As spatial symmetries dictate the protection of these surface states, not every surface can host protected surface states. Taking this into account we will find three different surfaces which can exhibit surface states, as these have the necessary symmetry group to protect these surface states. These are the (100), (110) and (111) surfaces. To see why these surface states exist we have to consider what spatial symmetries imply for a Hamiltonian.

In general, symmetries of a Hamiltonian are those of which the operator commutes with the Hamiltonian, that is to say with an operator S and Hamiltonian H we have $[S, H] = 0$. If this is the case, we can find a basis in which we get both eigenstates of H and S. This implies that H can be decomposed into a matrix with blocks on the diagonal, where each block corresponds to an eigenvalues of S.

To see what we consider when looking at these symmetries we will go over an example for a mirror symmetry with respect to the (100) plane. Lattice symmetries can generally be described as $UH(\mathbf{k})U = H(R\mathbf{k})$. For a (100) mirror symmetry we find that $UH(k_x, k_y, k_z)U^\dagger = H(-k_x, k_y, k_z)$, where U is a unitary operator. The reasoning for this requirement is that when we examine a state in the mirror only the movement perpendicular to the mirror inverts.

Spin, however, reacts differently. A sketch of what happens under mirror symmetries is given in Fig. 4. Here we see that the components that are not perpendicular to the mirror invert. If we combine these two we find that $U = e^{-i\frac{\pi}{2}\sigma_x} = i\sigma_x$. For this unitary operator, we can see that $U^2 = -1$, which lets us conclude that $U = \pm i$.

This operator lets us transform our Hamiltonian to a basis corresponding to U. In general, this would look like $H = \begin{pmatrix} H_+ & 0 \\ 0 & H_- \end{pmatrix}$, where $H_\pm$ are two new Hamiltonians describing the behavior of the eigenmodes of U. As these Hamiltonians are not coupled we can determine a mirror Chern number for each called N_+ and N_-. We can then calculate the Chern number by $N_+ + N_- = N$, however, the mirror Chern number $N_m = N_+ - N_-$ is also a topological invariant. What was found is that this mirror Chern number for SnTe is two instead of zero.
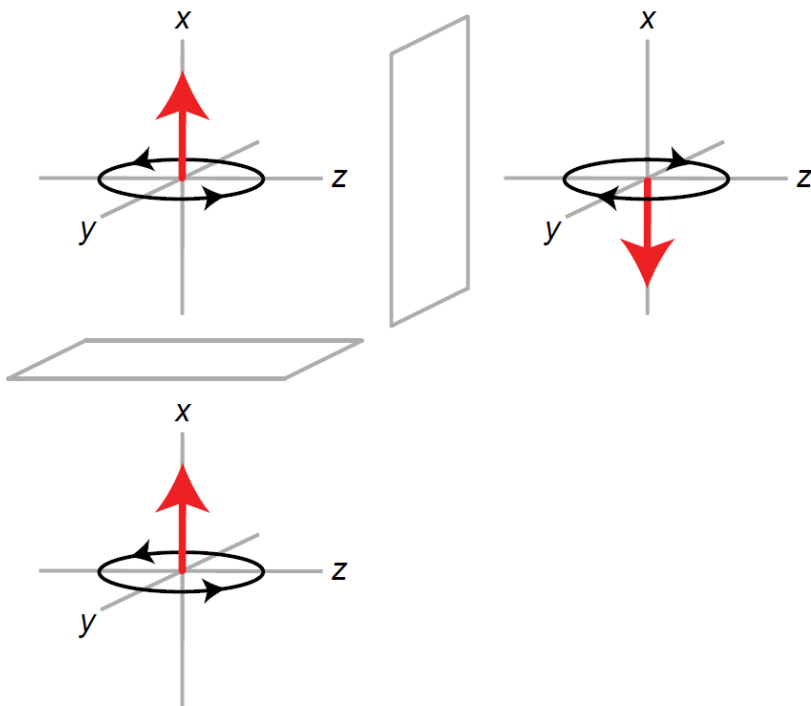

FIGURE 4: **Spin under mirror symmetry**
An illustration of the behavior of spin under mirror symmetry. The spin component which points along the normal of the mirror plane remains while the orthogonal components get inverted. Adapted from [19].

In a broader sense, we only have surface states on the surfaces that project multiple Dirac cones on top of each other. In other words, these are the surfaces for which the symmetries of the surfaces dictate that multiple TRIMs overlap. With the symmetries in the bulk, we find 3 different surfaces that can host the surface states. These are the surfaces (100) and (110), which have their TRIMs projected on each other by the mirror symmetry of the system. The (111) surface also allows surface states as this surface has the TRIMs projected on top of each other by the rotational symmetry around the [111] axis.

2.2.2 Two different kinds of surfaces

SnTe forms a lattice structure at room temperature that is similar to salt, which is called a face-centered cubic lattice. As mentioned earlier this brings with it a class of symmetries referred to as C_4. Considering the surfaces that we can create with such a lattice, we find that they give three different surfaces of interest where some of these symmetries are preserved. They are the (100), (110) and (111) surface. For SnTe now also consider that the Dirac cones are located at the L points, which are TRIMs located at $(\pm\pi, \pm\pi, \pm\pi)$ as seen in Fig. 3, then we find that at these high symmetry surfaces if we have overlapping Dirac cones when we project the Dirac cones on the surface. As we also have a non-zero mirror Chern number, these Dirac cones must close the gap, this ensures there must be two Dirac cones linked by mirror symmetry [20]. A graphical representation of these Dirac cones can be seen in Fig 5. This hybridization of the Dirac cones is only present for the surfaces that have Dirac cones projected on the same point, which are the (110) and (100) surfaces. The (111) surface also hosts topological states however it does not have these hybridized Dirac cones.

This implies that we have two kinds of surfaces. We have two surfaces, the (100) and (110) which host these hybridized Dirac cones [21]. However, then we also have the (111) surface which is also protected by mirror symmetries but does not have this hybridized cone. However, this surface still has four Dirac cones as do the (100) and (110) surfaces which are all protected by the C_4 symmetries of SnTe.
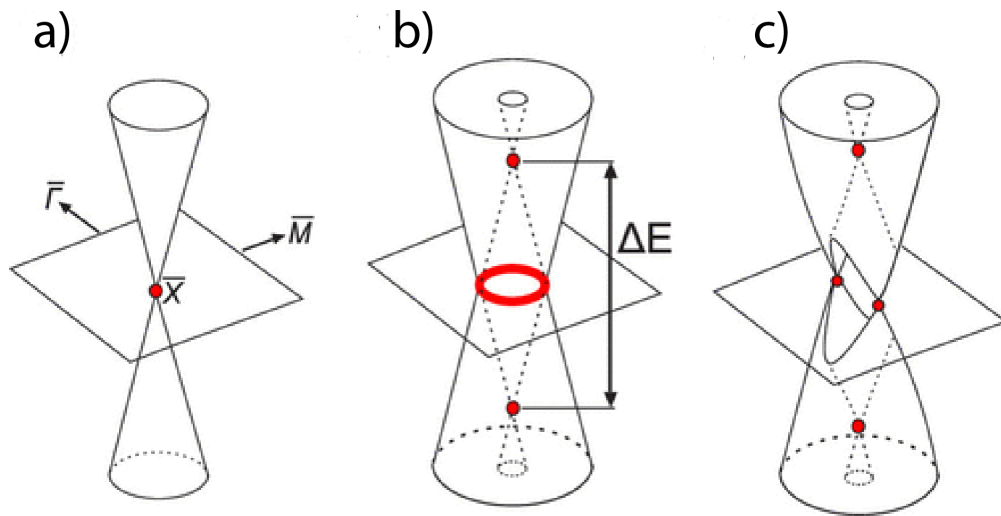
FIGURE 5: **Graphical presentation of Dirac cones in SnTe**
a) A single Dirac cone centered at the $\bar{X}$ point in the band structure. b) Two Dirac cones projected on the same place in k space but with different energies they are centered around. c) Hybridized Dirac cones in SnTe after the interaction between the Dirac cones has been taken into account. Adapted from: [22].
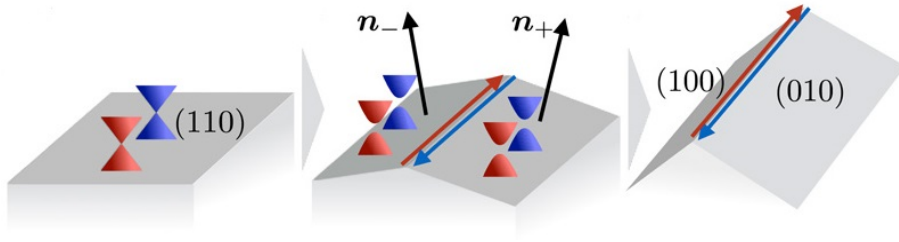
FIGURE 6: **Transition from surface to edge state**
From left to right, first we have the (111) surface which hosts two Dirac cones. Next, we bend this surface such that the surfaces have the normal $\mathbf{n}_-$ and $\mathbf{n}_+$. These both deviate equally from the surface normal of the (110) surface. As these surfaces do not have any of the symmetries of SnTe we find that the Dirac cones are gapped. This implies an energy where we will find edge modes but won't find surface modes. As we have T-symmetry in this example we find a Kramer pair of counterpropagating modes. Finally, we consider the bending going so far that we reach the (100) and (010) surfaces. Here we still have edge modes but as these surfaces have the crystal symmetries of SnTe we find that they can host surface states again. This figure is adapted from [6].

2.2.3 Edge states

SnTe is also predicted to have edge modes [6, 23]. These are generally called Higher-order topological insulator (HOTI) states as they are 1D states instead of the 2D states that are present for 3D topological insulators. In particular, these edge modes are also protected by symmetry due to the crystal symmetries present in SnTe.

We can consider a 2D surface that hosts surface states to sketch why these edge modes exist. For example consider the (110) surface for SnTe as given in Fig. 6. On this surface we have our Dirac cones hybridized and as it has the necessary symmetries it hence has surface states. As we bend this surface, we transition through surfaces that do not have the necessary symmetries and hence have a gap in the Dirac cone. Then once we arrive at the (100) surface we can again host surface states. However, our edge was able to host the modes from the (110) edge the entire time, which implies that it now hosts separate protected 1D modes.

3 Modeling SnTe using a k·p hamiltonian

In section 3.1 a k·p model will be specified for SnTe, which is examined subsequently in terms of the eigenvalues and eigenvectors of the Hamiltonian. In section 3.2 the Hamiltonian formulation is applied to a real space structure with a single surface. An expression for the energy bands is determined and an overview is given of when this material is topological non-trivial. In section 3.3 the model is applied to a slab geometry and numerical results are analyzed.

3.1 Setting up the low energy Hamiltonian

One of the ways to describe the behavior of topological insulators is by examining a low-energy model of the band structure. This model only takes into account the few bands that dominate the structure of the Dirac cone, while leaving out the bulk bands. One of the better-known models of this kind is the low energy approximation of the Topological Insulators (TIs) such as Bi_2Se_3, Bi_2Te_3 and Sb_2Te_3 [24]. This particular model has for instance been used to predict the effect of hybridization when considering a thin slab [25].

For SnTe a low-energy model has also been constructed and examined. On the topic of hybridization, a model of the form has been proposed given in equation 1 [26].

$$H_{hyb}(\mathbf{k}) = \tilde{m}\tau_z + (\tilde{v}_x k_x s_x - \tilde{v}_y k_y s_y)\tau_x \tag{1}$$

Here $\tilde{m} = \sqrt{m^2 + \delta_2^2} - |\delta_1|$, $\tilde{v}_x = v_x sign(\delta_1, \delta_2)$ and $\tilde{v}_y = \frac{v_y|\delta_2|}{\sqrt{m^2+\delta_2^2}}$ are constants where m describes the self energy, v_x and v_y describe a coupling between the Kramer pairs, while $v_{x'}$ describes the coupling between cation and anion. The constants δ_1 and δ_2 describe the coupling between the two (001) surfaces of SnTe. More specifically, δ_1 determines the intra-orbital hybridization strength between the cation and anion while δ_2 describes the inter-orbital hybridization strength. Moreover, s_i and τ_i represent Pauli matrices describing Kramers doublet and cation/anion (Sn/Te) respectively with $s_z = \pm 1$ and $\tau_z = \pm 1$. This model predicts that for films thinner than 5 atomic layers, SnTe loses its topological features on the (001) surfaces due to hybridization as the band gap inverts [26]. However, this model lacks the complete picture of the circumstances under which the material displays topological characteristics, and what the consequence of the form of the wave function is. To this end, it does not consider nonlinear terms for $\mathbf{k}$ which as will be shown in the next paragraphs is needed to examine the behavior of a TI for intermediate thicknesses. The aim of this chapter is to examine a model that encapsulates more features without considering more than four bands.

We start from the low-energy Hamiltonian by Hsieh et al. [4], which was derived from [27]. This Hamiltonian can be constructed based on the crystal symmetries of SnTe. The model by Hsieh et al. only considers linear terms in $\mathbf{k}$. We extend this model and include all terms up to and including the second order in $\mathbf{k}$ instead of only the first order. Suppose we would use the same model where only linear terms in $\mathbf{k}$ are included then we can only get solutions of the form $\Psi = \sum \psi e^{\lambda z}$, where λ is real. This would describe only the exponential decay of the wave function. When using second-order terms, λ can be imaginary. This translates to surface states which can have a wave character into the surface, next to the exponential decay. The original model by Hsieh et al. is

$$H_{Hsieh} = M_0\tau_z + v(k_1\sigma_2 - k_2\sigma_1)\tau_1 + v'k_3\tau_2 \tag{2}$$

with basis $\psi_{\sigma,\tau} = (\psi_{\uparrow,1}, \psi_{\uparrow,-1}, \psi_{\downarrow,1}, \psi_{\downarrow,-1})$. Here $\uparrow,\downarrow$ represents the total angular momentum in the r_3 direction, which is the [111] direction, while $\{-1, 1\}$ represents the behavior at the anion and cation. Here M_0, v, and v' are real parameters that can be fitted to a band structure. M_0 is a measure for the bandgap of the material, $v(k_1\sigma_2 - k_2\sigma_1)$ and $v'k_3\tau_2$ both give a coupling between the spin and the orbits. Each term does this concerning a different momentum direction. In addition, k_1, k_2, and k_3 form an orthonormal basis of vectors where k_3 points along the [111] direction and k_2 is in the $(1\bar{1}0)$ direction. This implies k_1 is in the $(11\bar{2})$ direction. Specifically for SnTe this implies that k_3 intersects one of the L-points and k_2 points along a surface with mirror symmetry. Compared to $H_{hyb}(\mathbf{k})$ we want to see if the inherent symmetries which are present due to the construction remain visible in the band structure.

If we compare the Hamiltonian in 2 to the Hamiltonian in 1 we can see that these are largely similar with the exception of the last term for the Hamiltonian by Hsieh and the augmented parameters for the Hamiltonian derived by Liu et al. If we start with the Hamiltonian by Hsieh we have the advantage of keeping the k_3 term, which will come to represent the spatial distribution of the wavefunction orthogonal to the surfaces we consider. Hamiltonian 1 uses the parameters δ_1 and δ_2 to this extent which represent the amount of hybridization. However, how these exactly convert to a set number of layers/distance between surfaces has not become clear hence the approach with Hamiltonian 2 is chosen.

With the package Qsymm, which is a package in Python to construct low-energy Hamiltonians from symmetry constraints, we expanded the existing low-energy Hamiltonian [28]. This requires the symmetries of the system corresponding to the crystal of SnTe, to generate a corresponding low-energy Hamiltonian with parameters. We specified that all terms should be included up to the second order in $\mathbf{k}$, neglecting any terms that amount to the identity or contain higher-order $\mathbf{k}$ terms. This resulted in the terms of the linear Hamiltonian and an additional term expressed as

$$H_2 = (B_1(k_1^2 + k_2^2) + B_2 k_3^2)\tau_3 \tag{3}$$

Here B_1 and B_2 are real parameters, that give the wave characteristic of the wave function. Without this term, one would find decaying exponential solutions. By adding this term it is possible to also have standing waves as the solution. This is due to the quadratic dependence in $\mathbf{k}$ now present in the Hamiltonian. The standing wave characteristic is significant as the hybridization gap in the dispersion relation scales with the overlap of the surface states of both sides, which can now acquire an oscillatory component. This oscillatory component will only make the overlap smaller or invert it entirely. With this in mind, it is not a stretch to hypothesize that this will decrease the gap in the model compared to one where there is no oscillatory component.

The Hamiltonian given in equation 2 can be expressed as a matrix. As σ_i and τ_i describe independent spaces we can rewrite a multiplication of those by the Kronecker-product of the two. This produces a space where the basis consists of both the σ_i and τ_i basis vectors. If we do this for the entire Hamiltonian we get

$$
\begin{aligned}
H_T &= H_{Hsieh} + H_2 \\
&= \begin{pmatrix}
M(\mathbf{k}) - B_2 k_3^2 & -iv'k_3 & 0 & v(ik_1 + k_2) \\
iv'k_3 & -M(\mathbf{k}) + B_2 k_3^2 & v(ik_1 + k_2) & 0 \\
0 & v(-ik_1 + k_2) & M(\mathbf{k}) - B_2 k_3^2 & -iv'k_3 \\
v(-ik_1 + k_2) & 0 & iv'k_3 & -M(\mathbf{k}) + B_2 k_3^2
\end{pmatrix}
\end{aligned} \tag{4}
$$

where $M(\mathbf{k}) = M_0 - B_1 k_\perp^2$. Here, we define $k_\perp^2 = k_1^2 + k_2^2$. All constants are taken to be real as their units are given in eVÅ and eVÅ^2 for (m, v', v) and (B_1, B_2) respectively.

In general, it is not possible to have an analytical solution for this Hamiltonian. Hence, we will follow the steps by Asmar et al. to make the necessary approximations to find the effects of hybridization [25]. We will also consider the Dirac cone, which this model aims to describe, to be located at the L-points of the Brillouin zone for SnTe and not at the Γ-point as is the case for Bi_2Se_3, as this is the case for these materials. Hence, we will shift our Hamiltonian such that $\mathbf{k}_{H_T} = \mathbf{k}_\Gamma - \bar{\mathbf{k}}_L$. Here, $\mathbf{k}_{H_T}$ is the momentum with respect to the L-point, $\mathbf{k}_\Gamma$ the momentum with respect to the gamma point in the Brillouin zone and $\bar{\mathbf{k}}_L$ the location of the L-point in the Brillouin zone when considering SnTe. As this is a translation of the coordinate system of the Hamiltonian, this will not affect the band spectrum.

Coincidentally this Hamiltonian also provides an approximation for the topological insulator Bi_2Se_3 with the exception that this material has its Dirac cone around the Γ-point instead of the L-point [24]. This Hamiltonian is not constructed from the symmetries present but by considering the most important bands. For SnTe, τ and σ in H_{Hsieh} correspond to the p-orbital on the cation (Sn) or anion (Te) and total angular momentum. In the case of Bi_2Se_3, they instead correspond to parity and spin respectively. Another difference between the two Hamiltonians is found in the definition of k_1, k_2, and k_3 as for Bi_2Se_3 these are defined as k_x, k_y and k_z respectively.

As a first configuration, we will consider a single surface geometry which will then be extended to a slab geometry. Hence, the solutions we are looking for are planar waves in the r_1 and r_2 directions while evanescent in r_3. We take $k_1, k_2 \in \mathbb{R}$ and $k_3 \in \mathbb{C}$ The reasoning being that in the r_1 and r_2 direction, we have an infinite plane, hence we expect Bloch waves which correspond to real k_1 and k_2 values. In the r_3 direction, we want to allow for possible decaying waves. These choices yield a momentum operator that is self-adjoint and yields a valid eigenproblem with real energy results, to be solved [29].

To examine the eigenfunctions of this system we make use of the trial function

$$\psi_{\sigma,\tau}(\mathbf{k}, \lambda) = (\psi_{\uparrow,1}, \psi_{\uparrow,-1}, \psi_{\downarrow,1}, \psi_{\downarrow,-1})_\lambda e^{k^\perp \cdot r^\perp} e^{\lambda r_3} \tag{5}$$

This trial function assumes a planar wave in the $r = (r_1, r_2)$ direction while the behavior in the r_3 direction may show evanescent or oscillatory behavior. The latter direction will be orthogonal to the surface. It is convenient to use the fact that H_T commutes with the helicity operator $\hat{h} = (\sigma \times \mathbf{k}) \cdot \hat{r}_3 / k$ [30]. We take the helicity with respect to r_3, which points along the [111] direction. This results in eigenvalues ± 1. Each surface will be described by its helicity so we aim to find these eigenmodes.

Next up we use the Hamiltonian (4) on the trial function (5). This results in an eigenvalue problem with the trial function an eigenvector of the Hamiltonian. The eigenproblem can be described as

$$\det(H(k_1, k_2, -i\partial_{r_3}) - EI_4) = 0 \tag{6}$$

where we made the substitution $k_3 = -i\partial_{r_3}$ to replace the momentum k_3 by the momentum operator which we can apply to our trial function. This gives the solution for λ which is

$$\lambda_{\alpha,\beta}(k^\perp, E) = \beta \sqrt{\frac{-2B_2 M(\mathbf{k}) + v'^2 + \alpha(-4(k^\perp)^2 B_2^2 v^2 + 4E^2 B_2^2 - 4M(\mathbf{k})B_2 v'^2 + v'^4)^{1/2}}{2B_2^2}}$$

Here, $\alpha, \beta \in \{-1, 1\}$. The α and β originate from the 4th-degree polynomial which results from equation 6. To avoid errors in the derivation, the symbolic manipulation module of Matlab was used throughout this chapter. In this equation, E is an eigenvalue of the Hamiltonian, and the real part of λ is the penetration depth of the wave.

From this result, we can distinguish that λ takes a couple of forms. Either we have a complex conjugate λ_β pair or we have a λ_β pair that is entirely real or imaginary. We can also determine the corresponding eigenvectors, albeit dependent on the eigenvalue E. This gives eight basis functions in total as there are a total of four λ values with two unique vector functions, one for each surface.

$$\psi_{\alpha,\beta,1} = \begin{pmatrix} \lambda_{\alpha,\beta}v' \\ \sqrt{(B_2\lambda_{\alpha,\beta}^2 + M(\mathbf{k})^2 + \lambda_{\alpha,\beta}^2 v'^2 + (k^\perp)^2 v^2} - B_2\lambda_{\alpha,\beta}^2 - M(\mathbf{k}) \\ v(-ik_1 + k_2) \\ 0 \end{pmatrix} \tag{8}$$

$$\psi_{\alpha,\beta,2} = \begin{pmatrix} -\sqrt{(B_2\lambda_{\alpha,\beta}^2 + M(\mathbf{k})^2 + \lambda_{\alpha,\beta}^2 v'^2 + (k^\perp)^2 v^2} + B_2\lambda_{\alpha,\beta}^2 + M(\mathbf{k}) \\ -\lambda_{\alpha,\beta}v' \\ 0 \\ v(-ik_1 + k_2) \end{pmatrix} \tag{9}$$

Which gives the general solution for the wave function

$$\Psi(r_1, r_2, r_3; E, \mathbf{k}) = \sum_{\alpha,\beta,\nu} C_{\alpha,\beta,\nu}\psi_{\alpha,\beta,\nu}e^{k^\perp \cdot r^\perp}e^{\lambda_{\alpha,\beta}r_3} \tag{10}$$

where $C_{\alpha,\beta,\nu}$ are coefficients to be determined by the boundary and normalization condition. Here, $\nu \in 1, 2$ and $\alpha, \beta \in -1, 1$.

We will rely on the constants in Table 1 to predict the behavior of the surface states. These values were derived in [31] around one of the L-points. The other values correspond to a regular TI which will also be considered as a comparison [24]. We observe that both models satisfy the requirement that $M_0B_1 > 0$ confirming it to be a TI.

	SnTe	Bi$_2$Se$_3$
M_0	-0.07	0.28
B_1	-0.9	44.5
B_2	-4.5	6.86
v'	0.95	3.33
v	-2.4	2.26
$k^\perp$	10^{-8}	10^{-8}

TABLE 1: The values for the low-energy model when fitted to SnTe around the L-point and Bi$_2$Se$_3$ around the Γ-point. Here, $k^\perp$ has been set to a low value close to 0 as the gap is smallest at $k^\perp = 0$. The values have been adjusted such that they fit the definition of the Hamiltonian H_T [31].

3.2 Single surface state energy spectrum

In this subsection, we will consider a system that has a single surface where only possible surface states could exist. We enforce the following boundary conditions on the previously described model: We set the wave function to zero at the boundary where $r_3 = 0$. For $r_3 \to \infty$ we also require the wave function to go to zero, i.e., the real part of λ should be negative in this case. These conditions are represented by $\Psi(r_3 = 0) = 0$ and $\Psi(r_3 = \infty) = 0$, which represent a single infinitely extending boundary with normal vector $(r_1, r_2, r_3) = (0, 0, 1)$. When $r_3 > 0$, we will consider the Hamiltonian defined in 4 while for $r_3 < 0$ we have $\Psi = 0$.

With these boundary conditions, we observe that $C_{\alpha,1,\nu} = 0 \quad \forall \quad \alpha, \nu$ to yield $\Psi(r_3 = \infty) = 0$. This limits the wave function to cases with $\beta = -1$. Note that for the square roots in eq 7, we only consider the root with the positive real part due to β already covering the negative real part. Now we can set up a linear system to solve using the basis form specified earlier in eq. (10)

$$(\psi_{1,-1,1}, \psi_{-1,-1,1}, \psi_{1,-1,2}, \psi_{-1,-1,2})(C_{-1,-1,1}, C_{-1,-1,1}, C_{1,-1,2}, C_{-1,-1,2})^T = \mathbf{0} \quad (11)$$

where ψ are the different components of Ψ, C are the constants for eq. 10 and $\mathbf{0}$ the zero vector. This system represents the boundary conditions applied to the wave functions. As we have boundary conditions where the wave function amounts to 0, we can set up another secular equation as we are looking for non-trivial solutions to this linear equation, i.e., a solution for which $(C_{-1,-1,1}, C_{-1,-1,1}, C_{1,-1,2}, C_{-1,-1,2})^T \neq \mathbf{0}$. Defining a matrix $V = (\psi_{1,-1,1}, \psi_{-1,-1,1}, \psi_{1,-1,2}, \psi_{-1,-1,2})$, we get

$$\det(V(-i\partial_{r_3}, E)) = 0 \quad (12)$$

This results in the exact solutions

$$E = \begin{cases} \pm v k^\perp \\ \pm \frac{\sqrt{4(k^\perp)^2 B_2^2 v^2 - 4M(\mathbf{k})B_2 v'^2 + v'^4}}{2B_2} \end{cases} \quad (13)$$

Correspondingly, the λ values can be determined analytically. The first of these solutions is represented by figure 7. This shows a simple Dirac cone with slope v. The values we find for λ in this case are all distinct for each value of α and β which implies that the wave function corresponds to four linearly independent vectors. For $E = \pm v k^\perp$ we get

$$\lambda_{\alpha,\beta}(k^\perp) = \beta \sqrt{\frac{-2B_2 M(\mathbf{k}) + v'^2 + \alpha(-4M(\mathbf{k})B_2 v'^2 + v'^4)^{1/2}}{2B_2^2}} \quad (14)$$

for $E = \pm \frac{\sqrt{4(k^\perp)^2 B_2^2 v^2 - 4M(\mathbf{k})B_2 v'^2 + v'^4}}{2B_2}$ we get

$$\lambda_{\alpha,\beta}(k^\perp) = \beta \sqrt{\frac{-2B_2 M(\mathbf{k}) + v'^2}{2B_2^2}} \quad (15)$$
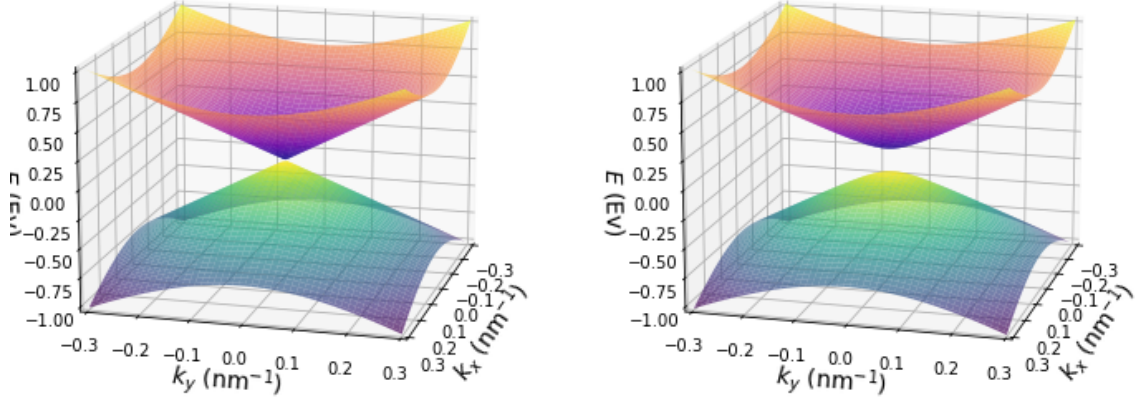
FIGURE 7: **Single surface Dirac cone**
The acquired solution to the single surface boundary problem with the given Hamiltonian. Left corresponds to the first case of Eq. 13 for SnTe while the right figure corresponds to the second case.

We can see that λ is either a purely imaginary or a real number, depending on the value of α in the latter case for E. This formula is linear in the large $k^\perp$ limit and has a gap at $k^\perp = 0$. This is the structure of a gapped Dirac cone. Likely this structure belongs to the bulk states of the model, which need to be present as without them there would be no inversion of the bands at the Dirac point. If we examine the corresponding eigenvectors, we see a degeneracy in the system as two of the eigenvectors are equal. To be more specific we have that $(\psi_{1,-1,\nu} = \psi_{-1,-1,\nu})$ for all ν, resulting in the determinant in eq. 12 being equal to 0.

We continue with determining the wave functions that correspond to the Dirac cone. While this can be done analytically, we instead opted for the numerical route as this should be easier to evaluate. This implies that we have to find all $C_{\alpha,1,\nu}$ such that eq. 11 is not solved by trivial solutions. This implies that we want to determine the nullspace of the matrix V. Finding an exact nullspace is not possible due to rounding errors. Instead, we find approximate solutions using singular value decomposition (SVD). With SVD we can decompose the matrix V as $V = \mathbf{U}\Sigma\mathbf{W}$, with Σ containing the singular values on its diagonal. The matrices $\mathbf{W}$ and $\mathbf{U}$ contain an orthonormal basis of vectors which are the right-singular and left-singular vectors respectively.

The matrix V is square, enabling a decomposition $V = \mathbf{U}\Sigma\mathbf{W}$ in which $\mathbf{U}$ and $\mathbf{W}$ are also square matrices, with a determinant equal to 1. Hence the determinant of V is equal to the determinant of Σ, i.e., it is given by the product of all singular values. This implies that we have a nonempty nullspace if one of our singular values is zero. As the singular values are ordered in the matrix from largest to smallest, we only need to examine the last singular value and verify whether this approaches zero. If so, we can construct the nullspace of the matrix by taking the corresponding vector from $\mathbf{W}$, here we do assume that only one singular value approaches zero instead of multiple. This is assumed as there are no degeneracies expected from the construction of the Hamiltonian. In the case where we try to solve $\det(V(k_3, E)) = 0$ numerically, we take the right-singular vector $\mathbf{w}$ corresponding to the last singular value as the nullspace and hence the solution to the original system of

equations. As we are only interested in the nontrivial solutions of eq. 11 we can discard the remaining singular values and vectors.
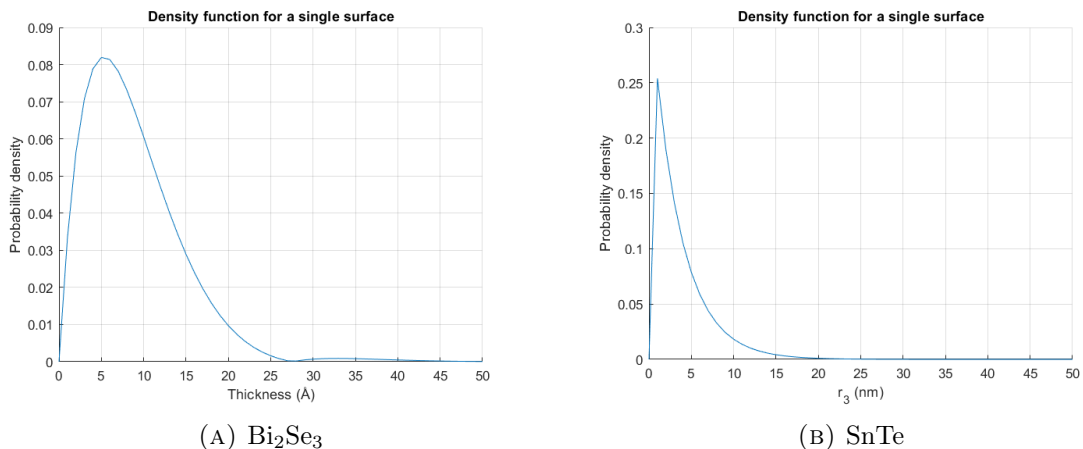

(A) Bi_2Se_3 (B) SnTe

FIGURE 8: **Single surface density function** Bi_2Se_3 **and** SnTe
A plot of the probability density corresponding to $k^\perp = 0.01$ in the Dirac cone for Bi_2Se_3 (left) and SnTe (right). The singular values of $6.9767e-16$ and $1.1622e-15$ were calculated corresponding to these solutions which can be regarded as zero except from machine precision.

In figure 8 the computed wave function can be seen. For Bi_2Se_3 we see a function with an exponential decay which occurs due to the trial function being a decaying exponential for negative λ values. Notice that around 27 Å we find that the probability density becomes zero and afterwards increases. This is due to the imaginary component of the λ values. As the λ values are complex conjugates we expect the resulting function to exhibit a periodicity at which it becomes zero. This occurs as the trial functions used are exponentials. If our λ values are complex conjugates we can rewrite them as a decaying exponential multiplied by a sinus function, of which the latter will attain a zero periodically. Finally, for this calculation, we get a singular value of the order 10^{-16}, which is close to the machine's precision. The wave function values are comparatively high, which implies that we have an accurate solution to our problem.

For SnTe we can also distinguish the boundary condition for $r_3 = 0$ and an exponential decay in the positive r_3 direction. We notice that the decay of the wave function is slower with a 'tail' that penetrates deeper into the bulk. We can check the exponential decay of this tail by taking the logarithm and extracting the slope of the figure. While we have the values in Table 1 which give the values for $\lambda_1 = -0.0838$ Å^{-1} and $\lambda_2 = -0.9760$ Å^{-1}, the actual decay of the wave function has a penetration depth of approximately 3.4 nm. The figure showing the logarithmic plot of the wavefunction can be found in appendix A. This is a higher penetration depth than is usually found for topological insulators, for example for common topological insulators such as Bi_2Se_3 and Bi_2Te_3 on finds around 1 to 10 Å [25].

3.3 Thin slab boundary conditions

In this subsection, we will consider a system with an infinite slab geometry with a given thickness L. Roughly speaking, each surface state is linked to the surface state on the opposite surface if the thickness of the slab is small enough. When we consider a thin slab

the wave functions associated with each side will overlap each other. The interaction of the wave functions due to this overlap is referred to as hybridization and is linked to a gap in the Dirac cone. Such a gap would imply zero transport for the specific energy levels within the gap.

Outside the slab, we will consider the wave function to be 0 to have proper surface states. For this purpose, one may assume the entire slab to be located inside a square potential well of infinite height. This setting can be represented by two Dirichlet boundary conditions, i.e., $\Psi(r_3 = 0) = 0$ and $\Psi(r_3 = L) = 0$. For $0 < r_3 < L$ we will consider the Hamiltonian H_T in eq 4 while outside of this range, we will consider the wave function to be 0. This gives us a linear system similar to equation 11. However, for the slab geometry, an 8x8 matrix is required to represent the system. We cannot solve for the energy E analytically as a function of $k^\perp$ or r_3. Instead, we aim for a numerical analysis based on a similar numerical scheme as used for the single surface case in the previous subsection.

First, a linear system is constructed representing the bulk problems as well as the two boundary conditions. From this system, a matrix V can be determined such that $VC = 0$ where C is a vector containing all coefficients of the general solution. We approximate the nullspace of the matrix V using SVD for a given r_3 by determining the vector that corresponds to the smallest singular value. Finally, we minimize this smallest singular value by a variation of E. We use the material parameters in table 1. This will give us a resulting E value for a given slab thickness.

For the minimization of E, first, an interval is determined in which the minimum is located. This is done by searching for the first local minimum starting at $E = 0$ in the positive direction. At each step, the singular value is checked. When the singular value is increasing for the first time, while it was decreasing in the previous step we note the interval between those values for E. After this, we will use the golden section method to narrow the interval until a tolerance for E of 10^{-10} is achieved.

The golden section method is an algorithm that can be used to determine a local minimum given an interval [32]. This is done by dividing the interval into 3 subintervals according to the golden ratio. At the border of these subintervals, the value of the function is calculated, i.e., the smallest singular value of V. In the next step, a new smaller interval is chosen in which we know the minimum to be present. The new interval is chosen by checking the smallest singular value at the two inner borders and comparing which one is larger. The E belonging to the larger of the two values is chosen as the new end of the interval on the corresponding side. This process continues until the remaining interval is small enough according to the tolerance.
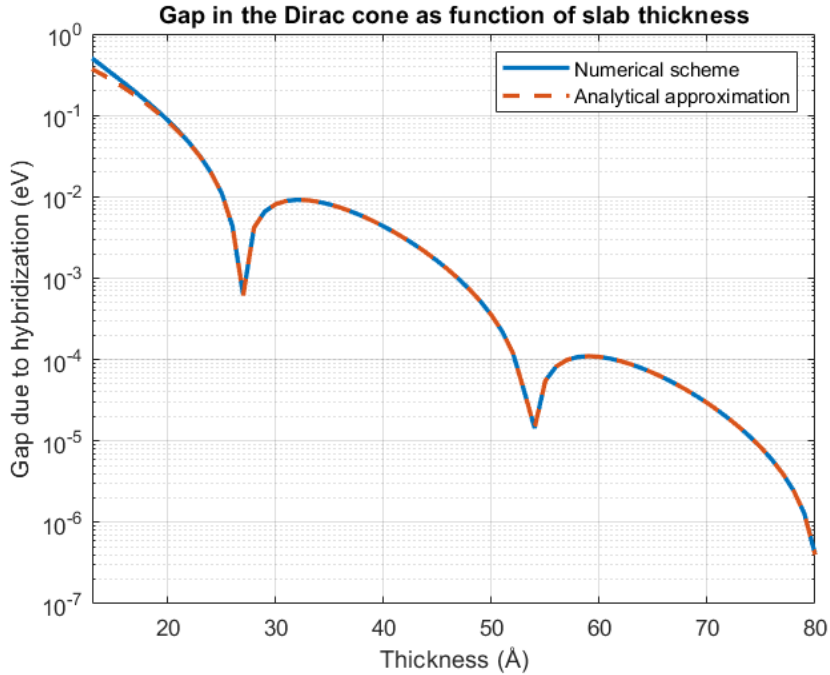
FIGURE 9: **Energy gap as a function of the slab thickness.**
A logarithmic plot of the energy gap as a function of the slab thickness given in units of 2a with the trivial and topological regime indicated. The gap is computed at $k^\perp = 10^{-8}$, which is assumed to be sufficiently small to have a negligible effect on the energy gap while being nonzero to prevent computational problems when calculating the singular values. The analytical approximation that is given is from [25].

In figure 9 we plotted the energy gap as a function of the thickness of the slab. The energy gap is calculated at $k^\perp = 10^{-8}$ as this is estimated to be close enough to 0 to find an accurate gap. This was done by considering the magnitudes of the other factors involved and then taking a number which is far less. If $k^\perp = 0$ is chosen, we are not able to compute a value for E as $\det(V)$ will always be 0. As the energy spectrum will be closely resembled by a Dirac cone with a linear dispersion as given in Fig. 7 the error by choosing a nonzero $k^\perp$ should be of the same order which is far smaller than the values present in the calculations. To check $k^\perp = 10^{-6}$ was also tried, this did not give a visual change in Fig. 9 up to a thickness of $70 * 2A$ Å after which it diverged from the analytical approximation.

Figure 9 shows the energy gap in the slab geometry as a function of the slab thickness $2a$. This energy gap is a consequence of hybridization, which amounts to the wave functions linked to each surface of the slab to overlap with each other. In the figure, we see around $r_3 = 27 * 2a$ Å and around $r_3 = 54 * 2a$ Å that the bandgap closes. When this happens, increasing a implies that the bands are inverted and a transition arises from the trivial regime, i.e., no edge states, to the topological regime, i.e., edge states exist. After a increases more the gap will close again such that the system will be topological once more. This pattern of oscillating between a trivial and nontrivial system will continue. While this effect persists for large thicknesses, the gap eventually becomes small enough to not have a significant impact on the band structure. The numerical model is also compared to

the analytical model [25]. We can see that the numerical predictions correspond quantitatively very closely with the analytical model. The largest deviation arises at small slab thicknesses, which is likely due to the approximation made for the analytical model which works in the limit $\sqrt{\frac{m}{B_1}} >> |\lambda(k^\perp, E)|$ as λ becomes greater when E becomes greater. The close correspondence with the numerical findings shows the validity of the numerical and analytical approaches taken.

Representation of the wave function in different slabs along r$_3$
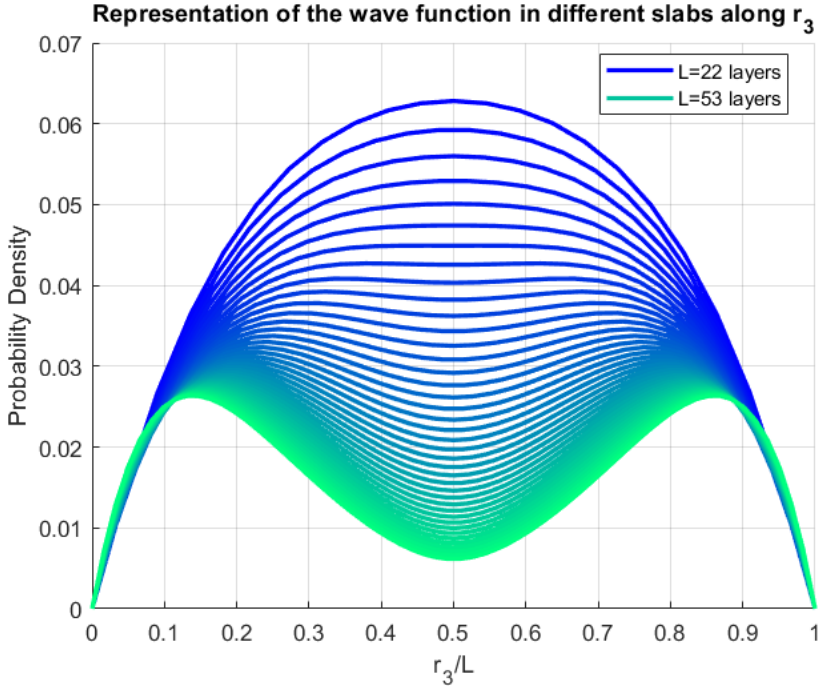
FIGURE 10: **Wave Functions for different slab thicknesses in** Bi_2Se_3
Wave functions w.r.t. different slab thicknesses. At each of the slab thicknesses, the wave function is 0 at both ends and is normalized along the x-axis w.r.t the thickness L of the slab. The colors transition corresponding to the thickness of the slab. Note that the wave function has been normalized concerning the thickness of the slab, hence states for thinner slabs have higher probability densities.

The wave functions obtained are given in Fig. 10. In the plot, we distinguish between thin slabs indicated by the blue lines, and thick slabs, indicated by the green lines. For a single surface, we would expect the wave function to look like Fig. 8. We can see for the green functions two of these functions on each side of the slab in Fig. 10 while for the thin slabs, we are not able to see any exponential decay. Instead, the wave function is maximal in the center of the slab. What we cannot see is if the function crosses 0 as was seen in the single surface case at $r_3 = 27 * 2a$ Å although it does seem to approach this. For a far thicker slab this should eventually approach it however.
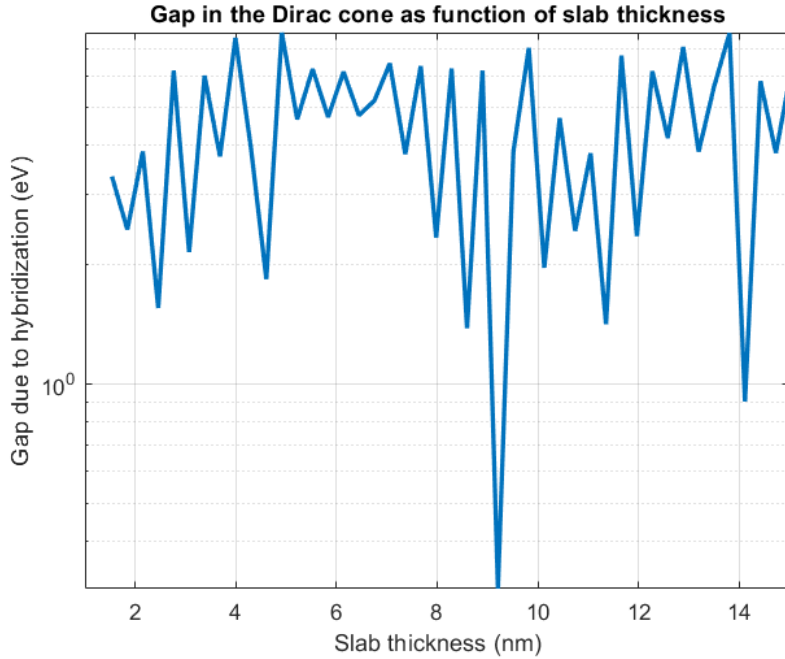
FIGURE 11: **Gap in the Dirac cone for SnTe**
Gap calculated for SnTe in eV. The gap is computed at $k_\perp = 10^{-8}$.

The predicted gap as a function of slab thickness for SnTe is presented in Figure 11. What we immediately see is that the gap we find is entirely different from the one in Bi_2Se_3. For SnTe the gap seems to depend in a very complex manner on the slab thickness while for Bi_2Se_3 the gap showed a periodic component. The gap is also rather large here in general as it is above 1 eV for most thicknesses. This shows that there is a problem with this approach.

We can go a bit more in-depth by considering the value of $\zeta = A_1^2 - B_1 M_k$. If this value is larger than zero, the gap we expect is trivial instead of topological. In Fig. 12 we have defined the two regimes where the gap is topological versus trivial. Here we see that compared to Bi_2Se_3 and Bi_2Te_3 we should expect to see a trivial gap. This trivial gap is then also what we see in Fig. 11. We note that the values are rather close to the other regime. Possibly, these values are not correctly fitted or there is something missing from the model. This behavior could be related to the second Dirac cone which is present in the Brillouin zone as explained in Fig. 5.

As a check, we have the singular values plotted in Figure 13 for some of the lower slab thicknesses. We observe that all singular values are below 10^{-7}, i.e., all are very close to 0. This signifies that the numerical calculations do achieve the required low singular value as we would like to see if this approaches zero. If this were not the case singular values much higher than 10^{-7} would've been found which indicates that there is no singular value of zero present.
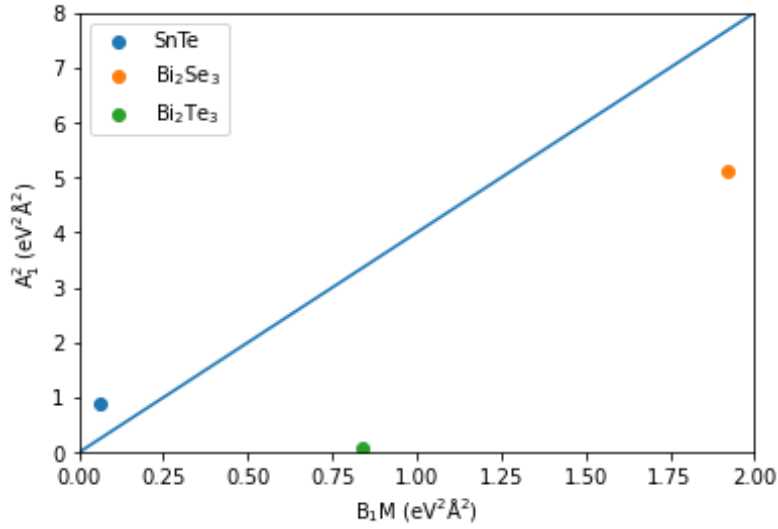
FIGURE 12: **topological and trivial regime for this low energy model**
A distinction between a trivial and topological gap. The trivial gap is expected
above the blue line while the topological gap is expected below. Notice that all
values do comply with the requirement of $B_1 M > 0$.

All in all, this shows that the model examined here does correspond to the literature for
parameters of Bi_2Se_3. However, when we consider appropriate parameters for SnTe we
find that this model does not show the topological regime of SnTe but instead the trivial
regime. This does not seem to be a calculation error but instead,d the origin likely lies in
the parameters used or some factor missing from the SnTe model.
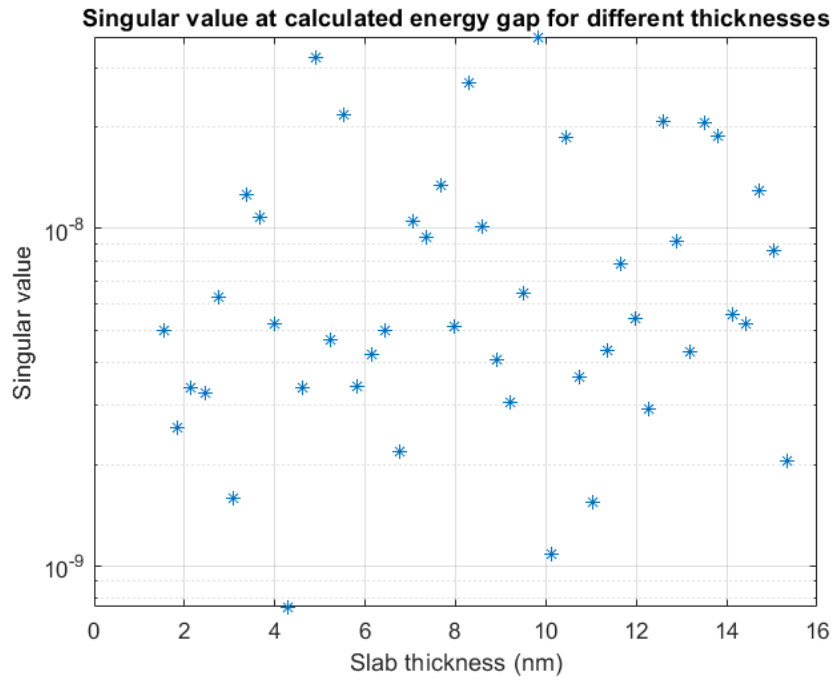
FIGURE 13: **Singular values for different slab thicknesses**
The singular values computed as a function of the slab thickness for $k^\perp = 10^{-8}$ for SnTe.

4   Modeling SnTe using the tight binding method

In subsection 4.1 you will find an overview of the tight binding model employed, in subsections 4.2, 4.3 and 4.4 the results of the tight binding model are shown with regards to the band structure, magnitude of the energy gap due to hybridization and (spin)-density plots in real space respectively.

4.1   The model

With the help of Kwant [33] a tight binding model will be implemented and examined for various shapes of a lead. Kwant is a package in Python that can create tight binding structures and perform calculations using these structures. To start, we need to define a Hamiltonian to use. We use the tight-binding model proposed by Hsieh et al. [4]. This model is represented in the following Hamiltonian.

$$
\begin{aligned}
H_{TB} = & m \sum_{j} (-1)^j \sum_{\mathbf{r},\alpha} c_{j\alpha}^{\dagger}(\mathbf{r}) \cdot c_{j\alpha}(\mathbf{r}) \\
& + \sum_{j,j'} t_{jj'} \sum_{(r,r'),\alpha} c_{j\alpha}^{\dagger}(\mathbf{r}) \cdot \hat{\mathbf{d}}_{\mathbf{rr'}} \hat{\mathbf{d}}_{\mathbf{rr'}} \cdot c_{j'\alpha}(\mathbf{r}) + h.c. \\
& + \sum_{j} i\lambda_j \sum_{\mathbf{r},\alpha,\beta} c_{j\alpha}^{\dagger}(\mathbf{r}) \times c_{j\beta}(\mathbf{r}) \cdot \mathbf{s}_{\alpha\beta}
\end{aligned}
\tag{16}
$$

where j=1,2 label the atoms Sn or Te, $s = \uparrow, \downarrow$ label the spin of the orbital, where an orbital are all possible energy levels considered on a single site, and $\mathbf{r}$ is the site position of the cubic lattice. c and $c^{\dagger}$ are the annihilation and creation operators corresponding to the three p orbitals p_x, p_y, and p_z as these orbitals have the most effect on the bands near the Fermi level [4, 34]. m describes the onsite potential which hence differs by only a minus sign for Sn and Te. This value is taken to be 1.65. $t_{jj'}$ describes the binding term between two lattice sites up to the next nearest neighbors. This implies we have four values t_{11}, t_{12}, t_{21}, t_{22} which are taken to be $-0.5, 0.9, 0.9, 0.5$. $\hat{\mathbf{d}}_{\mathbf{rr'}}$ describes the unit vector pointing from the site at r to r'. Finally, λ_j represents the spin-orbit term and is taken to be -0.7 [6]. For the spin-orbit coupling a Cartesian coordinate system was considered with a total angular momentum of $l = 1$, hence for the $L \cdot S$ spin-orbit coupling we use the substitution $L_j = i\epsilon_{jkl}$.

The general setup for the model will be an infinite lead with four surfaces as seen in Fig. 14b). The lead is infinite in the x-direction while the surfaces can be oriented in different ways to get particular facets. The most relevant surfaces are the (100) planes as these are the surfaces found for out-of-plane grown wires, hence these surfaces will mainly be considered for the infinite lead. We will consider the lead infinite in the [100] direction while the surfaces are formed by the (010) and (001) planes.
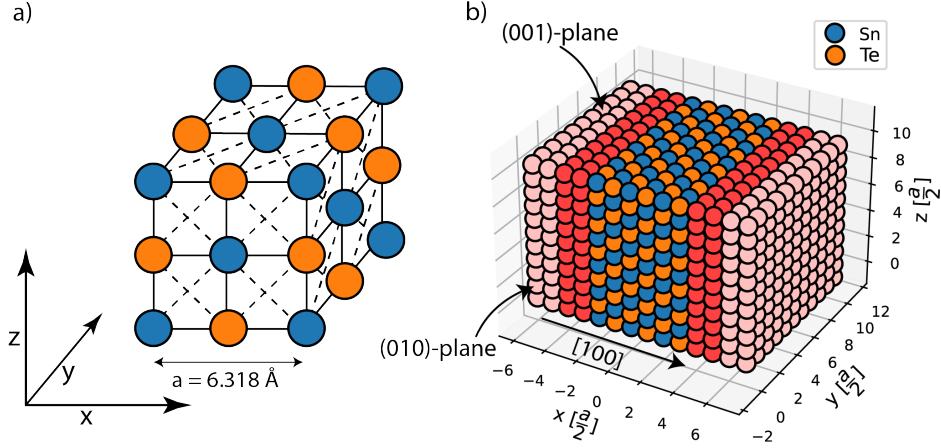
FIGURE 14: **General structure of SnTe**

a) The general lattice structure of SnTe where a=6.318 Åis the lattice constant of the unit cell. The solid and dashed lines give the nearest neighbor and next nearest neighbor bindings, respectively. b) An illustration of the lead used for calculations. The blue/orange bulk are atom sites at which the wave function is explicitly calculated. The red areas define the infinite lead, which has the same structure as the bulk while the pink areas are the infinite extensions in the [100] and [$\bar{1}$00] directions. The leads still consist of the same lattice structure as the bulk however they are infinitely extended by considering transversal symmetries. The planes describing the surfaces are the (010)-plane and (001)-plane.

As basis for the model a primitive cell consisting of two atoms was chosen, one Sn and one Te. The Sn atom would be in position (0,0,0) while the Te atom is in position (1,0,0). To extend this to the entire space we need to take into account that along the directions (1,0,1), (1,1,0), and (0,1,1) we have a translational symmetry for a cubic structure like SnTe. Using these translational symmetries Kwant is able to create infinite leads which extend into the [100] direction.

4.2 Band structure

We will examine the calculated band structure for energy levels around the Dirac cones. This is given in Fig. 15. Here the Dirac cones and bulk are shown in blue, where we have two Dirac cones, each the same distance from $k_x = \pi$. This corresponds to the Lifshitz transition described earlier as the L-points are projected at $k_x = \pi$. In between these Dirac cones we have the edge states. There are in total four distinct edge modes which are two times degenerate. We need one edge mode for each corner where we double this number once more as we have a spin degenerate system.
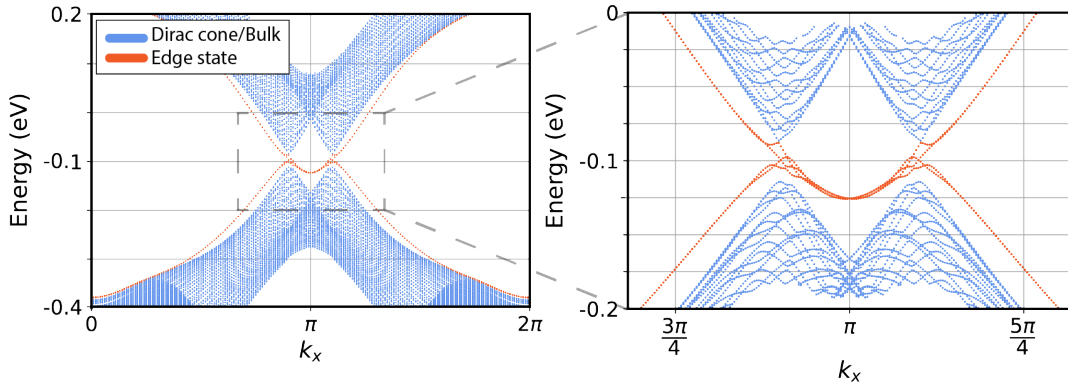
FIGURE 15: **Band structure of SnTe**
a) A full picture of the band structure of SnTe along the k_x direction for a lead with a 81x81 cross-section. The red bands are the bands that should host edge states. Notice that as this material is a TCI protected by mirror symmetry two Dirac cones present. b) A zoomed-in version of subfigure a. A small gap can be seen according to the hybridization of the surfaces of the lead. Notice the Dirac cones are centered around the L point.

In Fig. 15 we can see the top of the valence band around -0.35 eV. With a midpoint at approximately -0.1 eV this gives a band gap of approximately 500 meV. At 4.2 Kelvin the band gap for SnTe is about 300 meV, which only decreases as the temperature goes up [35]. This is caused by the model being fitted mainly to the Dirac cone and not the bulk band structure of the material. In the figure, the presumed edge states and surface/bulk states are highlighted. These edge states, as we will see later, have consistently shown a density around the edges of the wire throughout the calculations and have been highlighted similarly in other works [6]. The edge states were also consistently present throughout all calculations independent of the number of layers in the y and z direction. The form of the edge states however did change as the dimensions of the wire were changed.

4.3 The hybridization gap in the Dirac cone

The system we consider has a finite number of layers in the y and z direction, hence we have to consider hybridization. Due to hybridization, we get a gap in the Dirac cone. This gap in the Dirac cone can, just like for the surface states, host lower dimensional modes. These edge states can however only exist if the gap is topological, or in other words, if the mirror Chern number is nonzero.

The mirror Chern number is calculated in different ways depending on the symmetries of the system. The crystal symmetries mentioned earlier, which are a rotation symmetry around the [111] axis, a mirror symmetry with respect to the (110) surface, and inversion symmetry were defined for the bulk of the material. For our wire, these symmetries do not necessarily hold but subgroups of the symmetry group C_4 do remain.

In our case, we consider an infinitely long wire with (100) planes. The termination of these planes can be divided into two categories. Along an axis, we have Sn-Sn and Te-Te termination or we have Sn-Te and Te-Sn termination, which correspond to an odd and even number of layers respectively. If we have odd termination in both directions along our
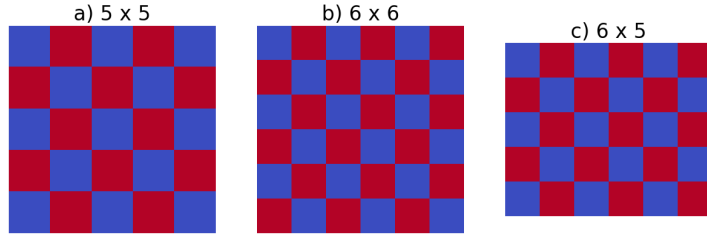
FIGURE 16: **Different symmetries for a 3D lattice**
An overview of the different types of crosssections for SnTe. a) gives the case of odd termination in both directions. b) gives the case of even termination in both directions. c) gives the case of even termination in one direction and odd termination in the other direction.

square wire, we have a wire that can be rotated concerning the [100] axis four times, which corresponds to a C_4 symmetry. We also have two mirror symmetries with respect to the surface that is orthogonal to a surface and is parallel to the [100] axis. Even termination in both directions interferes with this symmetry reducing it to a C_2 symmetry. In the last case, we can have odd and even symmetry in two different directions, here we do not have rotational symmetry but instead only mirror symmetry just like in the case with odd termination in both directions. All three cases are visible in Fig. 16.

Now the question quickly becomes, are we dealing with a topological regime or a trivial regime? For a 2D regime, we can consider the result in [36]. Given in Fig. 17 we can see the gap for an even and odd number of layers. We can see an oscillation with a period of about 60 Å taking place which suggests that a change in the mirror Chern number occurs when the gap is minimal.
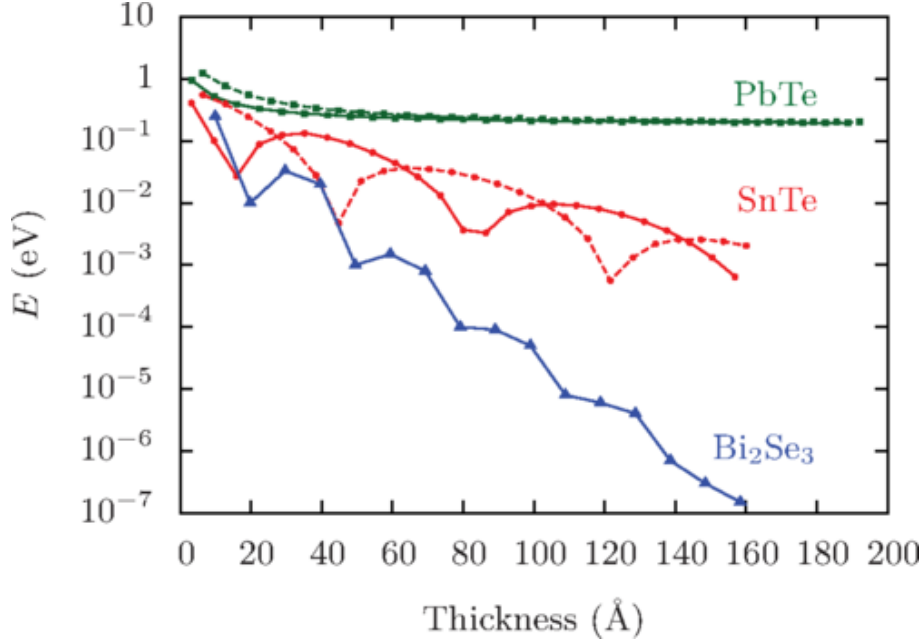
FIGURE 17: **Energy gap as a function of thickness**
Energy gap as a consequence of the hybridization of the surface states for thin films of nontopological PbTe (green), SnTe (red), and TI Bi_2Se_3 (blue) as a function of the thickness. The solid and dashed lines denote the magnitude of the energy gap for the odd and even numbers of layers, respectively. Adapted from [36].

With this figure, they also determined the appropriate mirror Chern numbers. This shows a change in the mirror Chern number indeed occurs. For odd termination they found the mirror Chern number oscillating between the values $N_M = \pm 2$. This implies that protected edge states are always expected, as they occur when the mirror Chern number is nonzero. For the case with even termination, the topological invariant changed between 0 and 2, starting at 0. This implies that for even termination the edge states are not always protected by crystal symmetries.

As these calculations were done for a 2D slab geometry, we can ask ourselves what this looks like for the wire geometry we consider. For the energy gap we took the smallest distance in energy when we only considered the bulk and Dirac cones, so not the four edge states, as given in Fig. 15. If we use this we can create a slab-like geometry.
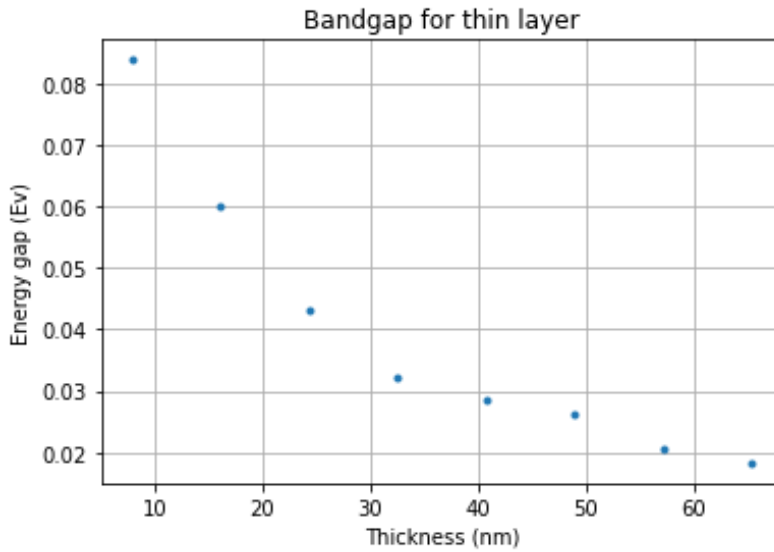
FIGURE 18: **Hybridization gap as a function slab width**
The figure gives the hybridization gap as a function length in the y direction of the slab while the length in the z direction remains 15 atoms (4.7nm). This lead was able to be a lot thicker due to the smaller height. Only odd termination was considered with intervals of 26 layers in between two datapoints.

In figure 18 a very thin 3D slab was considered of 15 atoms in length in the z direction with variable length in the y direction. This was created to check the hybridization gap as a function of the number of layers in the y direction instead of the z direction. As we can see, the band gap shows an approximate exponential decay as a function of the width of the slab. This is a consequence of the decrease in the overlap of the wave functions of the surfaces on each side. We can see that the gap decreases from about 0.08 eV to 0.02 eV. As the gap is still significantly decreasing for a width of 50 nm and more, we can determine that the penetration depth of the wave functions is very large, on the order of 10 nanometers.
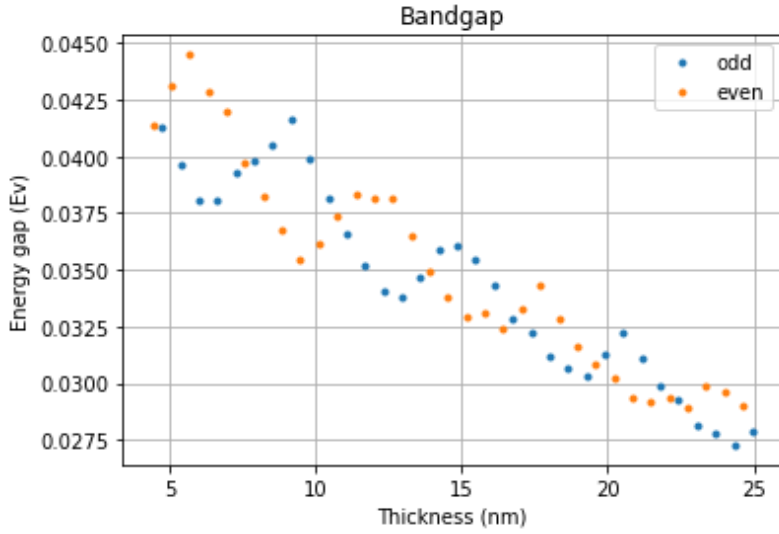
FIGURE 19: **Hybridization gap as a function of thickness in the z direction**
The figure gives the hybridization gap as a function of the thickness in the z direction
for a slab of width 79 atom sites (24.9nm). A distinction has been made between odd
and even thickness as they have different termination on the sides of the lead. Odd
termination has the same atom on each side while even termination has differing
atoms on each side.

A big downside in general with this method compared to a 2D slab is the time it takes
to do calculations. We have found that a cross-section of about 81x81 is the maximum
that can be achieved in a reasonable timeframe. Within these bounds, we calculated the
hybridization gap for a wire with a variable length in the y direction and a set number of
atoms in the z direction of 79 atoms. The results of which can be found in Fig. 19.

Here we see an oscillating pattern that is distinctly different for the even and odd layers.
This oscillating pattern has in both cases a period of about 7 nm, which is very close to the
period found in Fig. 17. Apart from this, we always have a rather large gap which almost
linearly decreases. This is attributed to the continuous hybridization that is present even
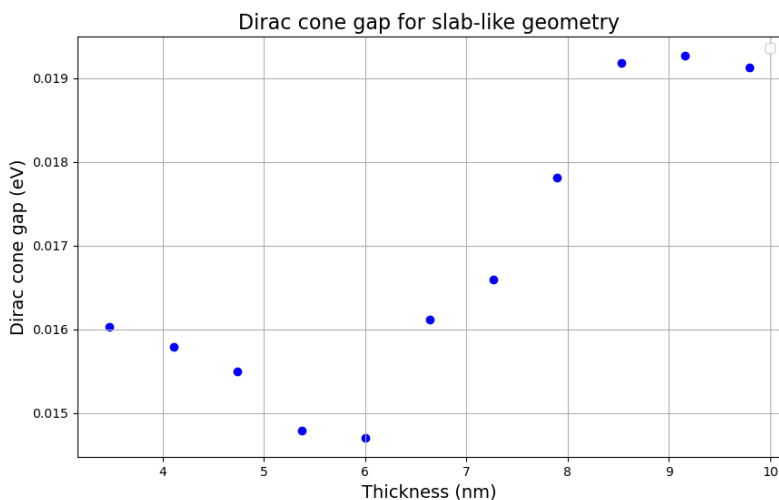in the direction which is 79 atoms or about 25 nm.

FIGURE 20: **Thin slab energy gap vs length in z direction.**
Energy gap in the Dirac cone due to hybridization of a thin slab with variable length
in the z direction. The number of atoms in the y directions of the 3D system is 201
atoms while the number of atoms in the z direction varies from 11 up to 31 layers
with odd steps.

We can also invert the direction that we want to change, as we did in Fig. 18. This results
in a setup where we already have a large width in the y direction, set at 201 atoms, and
variable height in the z direction. This approximates a thin slab model. The result of such
a calculation can be found in Fig. 20. As the model is a 3D model, we can only do these
calculations for small lengths. We chose to do this in the case of odd termination.

In the figure, we can see a minimum occurring around 6 nm, while for larger lengths the gap
increases instead of decreases. This range in lengths should account for about one period
in the periodic relation seen in Fig. 19. Hence we cannot explain this increase in gap by
suggesting that the increase on the left side of the figure will become much higher than
the peak on the right. Instead, we think the crux lies in the way the gap is determined.

As we increase in length the lowest part of the upper Dirac cone and the upper part of
the lower Dirac cone move. This movement is the main cause behind the oscillation in
the hybridization gap. If the amplitude gained by the energy gap due to this oscillatory
movement far outweighs the decrease we would see due to the hybridization between the
two opposite surfaces, we could see figures such as these.

4.4 Hinge modes in real space

Next, using Kwant, we can visualize the hinge modes in real space. This is done by plotting the probability density on a cut of the infinite lead. As the basis consists of two atoms, we will have to consider two layers in total to represent the whole wave function. The wave function itself is the eigenvector that belongs to a specific point on the band structure.
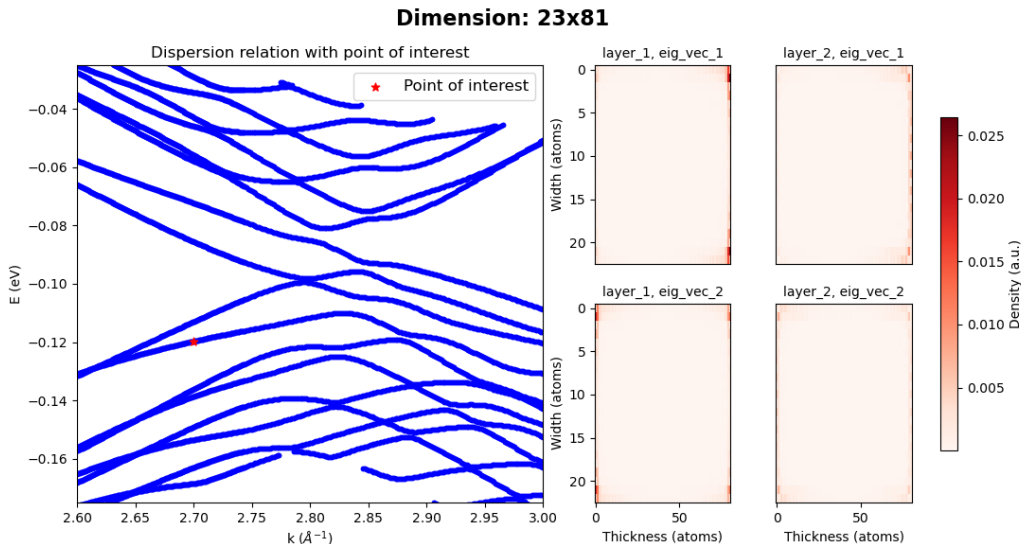

FIGURE 21: Dispersion relation (left) and the corresponding wave functions in real space (right). Each wave function corresponds to a layer and degeneracy pair. The probability density considered is at the lowest edge state for k=2.7.

In Fig. 21 we can see a band structure and the probability density. In total four cuts are given as we have a degeneracy of two due to a C_2 rotation symmetry together with the consideration that we need two layers to represent the entire wave function. In the figure, we can see a clear edge mode which is along the short axis distinct in each corner. One can notice that the edge mode is not entirely located on the edge, but instead is one site off. This edge mode also seems to be localized on the Te atoms instead of the Sn atoms.

If we compare the probability density in Fig. 27 to the one in Fig. 21, found in appendix B, we see that the former has its density located at the corner of the cross-section which corresponds to an Sn atom in the model. As Te is an anion while Sn is a cation in SnTe, Te can more easily provide free electrons to increase the conductance. Because of this, the lower two edge bands are both highest around the Te sites while the upper two bands have a wave function with its peak values at Sn sites. This also coincides with previous literature on the cation/anion character of the Dirac cone [37].

Problems arise when the k-point is closer to the gapped Dirac cone. An example of this is given in Fig. 22. Here still have edge mode contributions, given the asymmetry in the corners. However, we now also clearly see surface modes incorporated due to the proximity to the Dirac cone. These are suggested to be surface modes as the edge modes have been shown in Fig. 21 to be closely localized at the edges. At the same time, there seems to be no decrease in wave density from one edge to another which signifies a surface mode.

This suggests that the hybridization of the surface states not only changes the gap between the Dirac cones but also the character of the edge states in between the Dirac cone. This
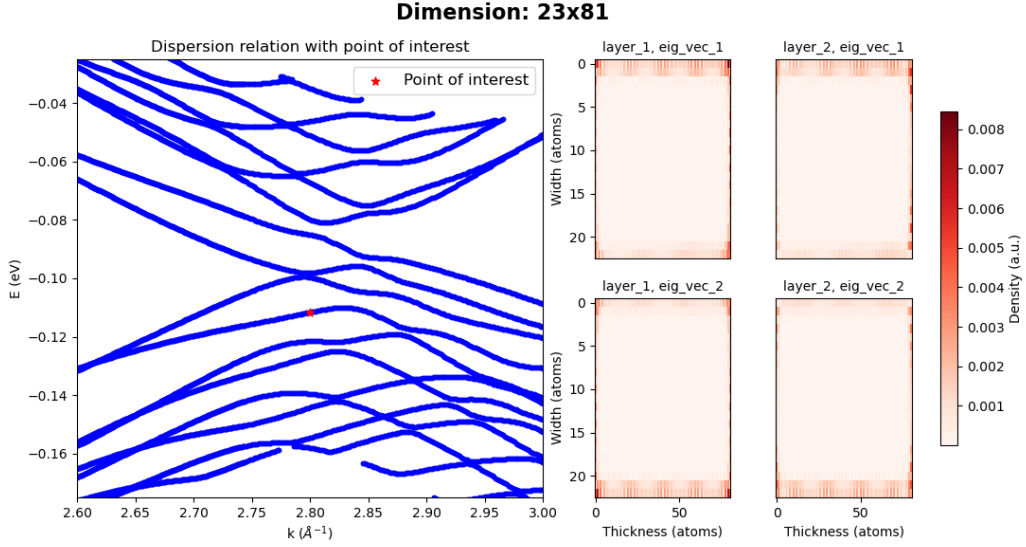
FIGURE 22: Dispersion relation (left) and the corresponding wave functions in real space (right). Each wave function corresponds to a layer and degeneracy pair. The probability density considered is at the lowest edge state for k=2.8. This value is close to the smallest gap found in the Dirac cone.

change is likely due to the gap closing and opening between the modes in the Dirac cone and the edge state which allows the character of the edge modes to change. This effect has also been previously seen when examined with the Aharonov-Bohm effect [38]. Here under the presence of a magnetic field the gap in the Dirac cone did not close but surface state behavior was seen on the edge modes.

We can also consider the edge mode on the right side of the Dirac cone, so near the L-point, which is given in Fig. 28 in the appendix B. Here we can see that just like in Fig. 21 and 27 the wave function density is located at the edges hence we define these as edge states.

We can also consider the spin density throughout the lead. This can be calculated within Kwant by applying the spin operator to the wave function. In total we have three directions for the spin, two are orthogonal to a face, which are the y and z directions. The last one is parallel to the direction of transmission.

In the case where we examine the spin in the direction of the lead, we find a spatial representation that suggests surface modes as can be seen in Fig. 29 in appendix B. However, as we can see, the spin density is small compared to the densities we found before. This suggests that this is instead a computational error.

What also strengthens this claim is the consideration of spin-orbit coupling in our Hamiltonian. In the case where we have spin-orbit coupling, we also have spin-momentum locking as a consequence. The momentum of the wave functions considered is in the k_x direction, spin-momentum locking then implies that the spin must be orthogonal to this direction, which would mean that the spin component in the x direction is zero.

If we consider the spin in the y direction we can see that we can see a symmetric spin component, as seen in Fig. 23. One of the eigenvectors corresponds to a spin on the right side of the material in the negative y direction. While the other eigenvector corresponds to a positive spin in the y direction but this time on the left side.
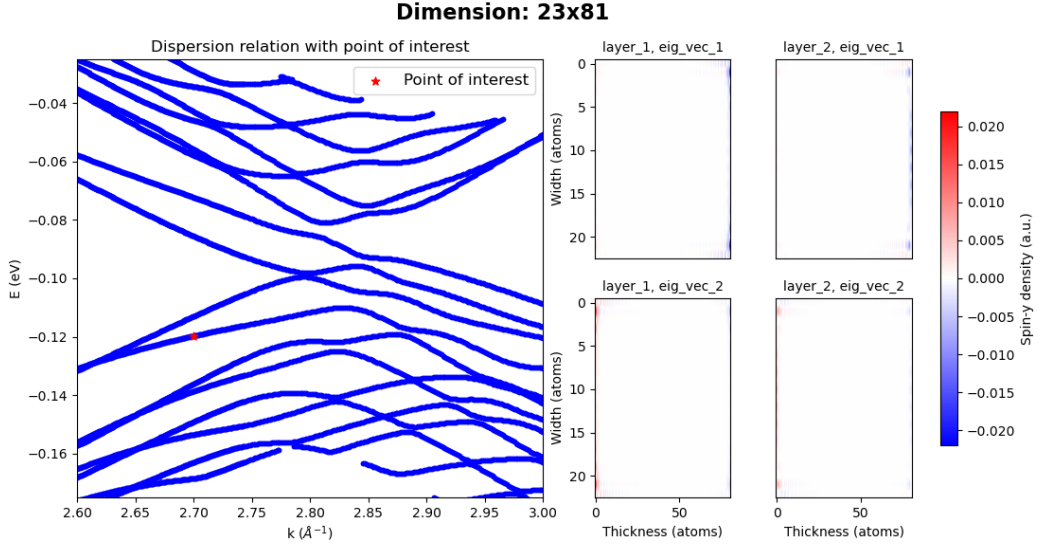
FIGURE 23: Dispersion relation (left) and the corresponding spin density in the y direction in real space (right).

This corresponds nicely with the mirror symmetry present in the system. For mirror symmetry, we have to take into account that the spin which is parallel to the mirror plane flips, which is the case here. One last thing of note is the presence of 2D-like states. These, unlike the components that point along the x direction, seem to be a lot more present along the smaller of the two surfaces. This implies that the states edge states cannot be regarded as separated in real space and hence can more easily interact with each other.

For completeness, we can also consider the spin density in the z direction for the wave function. This is given in Fig. 30. In this spin density plot, we also see the correspondence to mirror symmetry as we did with spin in the y direction, however this time it is with respect to a plane with a normal vector in the y direction. What is also noteworthy is the difference between the spin density in the y direction for the small surface compared to the spin density in the z direction in for the large surface.

For the small surface, we found a surface-like state which is especially visible for the spin in the y direction however no such spin density is present for any of the surfaces in the z direction. This seems to suggest that a surface that hybridizes will cause the edge states to connect by channels that correspond to the surface state in between the two edge states.
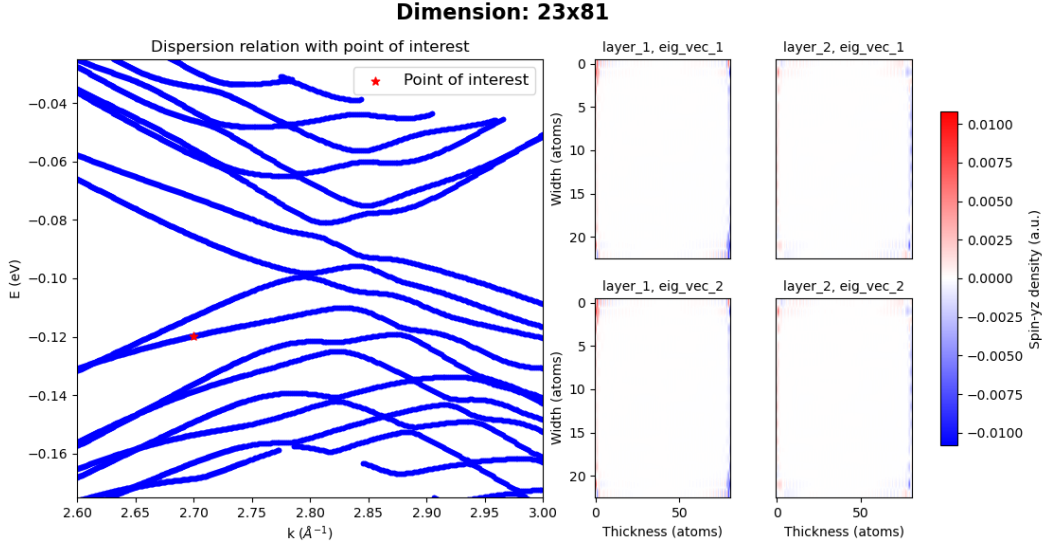
FIGURE 24: Dispersion relation (left) and the corresponding spin density in the y-z direction in real space (right).

We can also consider spin in a different direction than just x, y or z. An interesting direction for example is the spin which points in the yz direction. The resulting operator, which is $\sigma_{xy} = (\sigma_y + \sigma_z)/\sqrt{2}$ is proportional to the topological invariant for the edge states. This can be seen by considering that the mirror symmetry M_{yz} and $M_{y\bar{z}}$ are the topological invariants for the edge modes.

We can now focus on Fig. 24, where two of the edge states are clearly visible while the other two edge states are almost gone. In the case where we would not have hybridization, we expect that the edge states that do not correspond to the operator, would not be visible as the spin of the edge states are orthogonal. However, what we instead see is a small spin component in the other corners. This can be explained by considering that the hybridization of the two edge states changes the spin texture which makes the two states describing the edge modes not orthogonal anymore. Another point to consider is that the spin in the edge states is not only dictated by the location but also by the site, so Sn or Te. Which was also noted before.
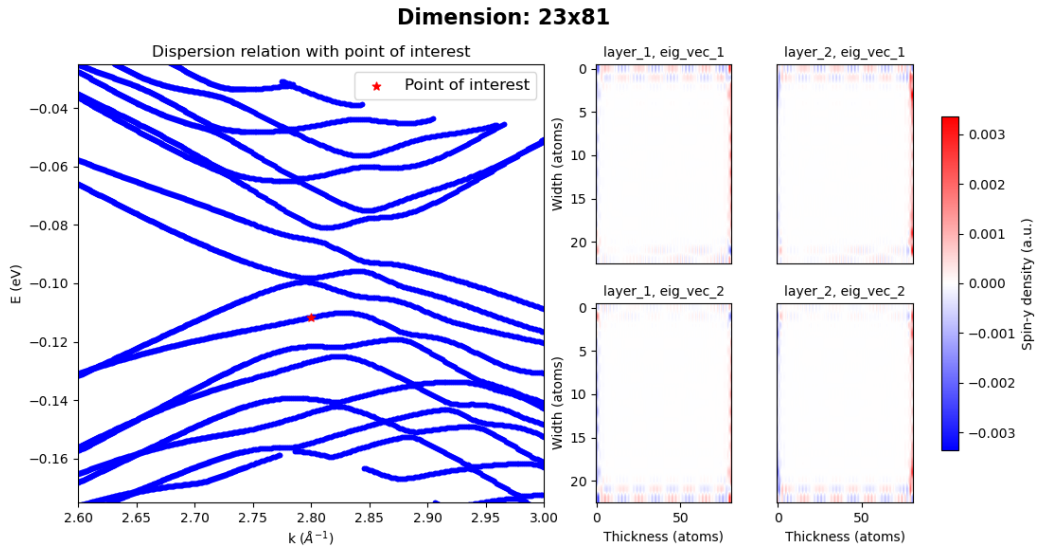
FIGURE 25: Dispersion relation (left) and the corresponding spin density in the y direction in real space (right). The point of interest in chosen such that the wave function is in between the tops of the Dirac cone.

Next, we consider a point of interest closer to the Dirac cone. This is given in Fig. 25 where we see an alternating pattern along the top and bottom surface. Physically these patterns will likely be irrelevant as the spin on the top and bottom surface averages out over both layers to be zero. Nonetheless, especially in the direction parallel to the top surface, we see a precession for the spin direction where it switches between up and down. Apart from this, the spin is locked to specific sites. On a single surface, the positive spin contributions are located on one kind of site, so Sn or Te, while the negative spin contributions are then located on the other kind of site. It could very well be that this is an artifact from the model implemented but it is hard to determine the exact origin of the precession.

Just like we saw in the case where we consider the spin in the y direction, in the z direction, as given in Fig. 31 we also see an alternating pattern, this time corresponding to the surface on the left and the right. The top and bottom surfaces also have oscillating behavior where the spin in the z direction increases and reduces, however, it never switches which corresponds to spin momentum locking. If we also consider both layers here we can see that on average over the two layers, the spin seems to be constant.

In [36, 39] they theorized that given a 2D model, one would always see edge states for SnTe in the case where we have odd layers. This coincides with the above calculations as the wavefunctions always have a character that shows to be more present around the edges instead of the surfaces. However, while these edge modes exist, we do see a mixing of the spins in the hybridization direction suggesting that these edge modes cannot be seen as totally separate. Besides this, they predict for an even number of layers that the edge states switch between a trivial and topological regime. This was not confirmed with these calculations. For all dispersion relations, as long as the dimensions of the wire were not too small, bands were seen in the dispersions relation which show a character centered around the edges of the wire. This is likely caused by the increased hybridization due to the edge and surface states which are, compared to the penetration depth, very near to each other.

5 Conclusion

In this thesis, two approaches have been compared to determine the influence of hybridization on charge transport in SnTe. The first one was an approach centered around a low-energy Hamiltonian of which the eigenvalues were examined under boundary conditions representing a 2D slab. The second approach is a tight binding model for which the energy gap in the Dirac cone was determined together with the wave density.

- First, we consider the low-energy model. The results of this model corresponded with the literature for the parameters of Bi_2Se_3. However, when the parameters of SnTe were used no clear gap in the energy was found. This was caused by the parameters used for SnTe, as they did not correspond to the topological regime but to a trivial insulator. The parameters were however shown to be close to the topological regime. This shows that an adjustment in the parameters could make this model work, assuming that the parameters can be fitted better. It was also determined that this model could be improved by considering the second Dirac cone present in the Brillouin zone too.

- Second, a tight binding approach was taken to SnTe with a focus on the (100) surfaces. This approach shows clear edge and surface states for the parameters used. The edge states and surface states were robust against the hybridization, i.e., their presence did not depend on the dimensions of the nanowire examined. The surface character was seen close to the Dirac point, even when the states in the bands determined to give the edge states were examined. This is explained by the character of these bands changing as a gap closed between the edge and surface state bands.

  The energy gap between the Dirac cones never closed entirely but instead remained rather large. As the gap was rather large for thick 3D slabs, the penetration depth is estimated to be in the order of 10 nm, although an exact numerical value could not be extracted. This implies that in thin slab devices and nanoribbons, it has to be taken into account that the energy gap will be larger due to hybridization compared to other TIs, for example, Bi_2Se_3.

  Finally in the density plots of the wave functions around the Dirac cone which should host edge modes, surface modes were spotted mixing in. These modes were less prevalent further away from the Dirac cones. These surface states in the edge states are a consequence of the hybridization of the surface states. Also when examining thin slab geometries, the wave density along the shortest axis had a large overlapping. This was especially prevalent when examining the spin along this direction. It shows that for devices on a nanoscale, edge states might not be entirely 1D but instead mix such that they form a surface-like state.

6   Discussion

We start by considering the low-energy approach to calculating the energy gap. This approach did not result in a clear energy gap in contrast to findings obtained with the tight-binding calculations. It was determined that this is caused by the parameters for SnTe which were not in the topological regime. The cause for this is twofold. The model did not take any mirror symmetries into account and hence it could be that this caused the model to show a trivial insulator. Another reason could be that the parameters were not precise enough as they are close to almost showing a topological regime. This could be solved by either of two approaches, one can in more detail calculate the parameters for this model and examine if this puts the model in the topological regime. The other option would be to expand the trivial model to include multiple Dirac cones for each surface.

The approach taken to calculate the wavefunctions for the low-energy model performed well as low singular values were recorded. Moreover, compared with another material, namely Bi_2Sn_3 the correspondence with an analytical model was very high. What this method however lacked was a way to determine the entire band structure. As the focus was to determine the energy gap, only the lowest band was calculated, but this prevented insight into the entire band structure. However, as this model only accurately predicts the lowest few modes not a lot of information was lost.

The tight binding model overall functioned well. The main caveat with this approach, which lies in the 3D nature of the model, is the memory usage for some calculations. With the resources available we could not go far beyond a structure of 81x81 sites as this would increase the time it took to get the eigenvalues by too much. When given more time, larger systems can be calculated when using sparse matrix methods. This does however also have a disadvantage. When the entire band structure is calculated one can algorithmically deduce which bands should be the edge states as these should correspond to the center 4 eigenvalues, in the case where we do not have all the eigenvalues but a select view such an automated algorithm could not be used. Also, the method where the entire wavefunction was calculated in Kwant was very memory intensive which prevented. This method not only determines the eigenvector but also calculates and summates all the eigenmodes at a certain energy level. As this leaves us with a 3D model which hybridizes in multiple directions no exact determination of the penetration depth could be done.

Nonetheless, the results showed edge state behavior in the density by only considering the channel. This, however, is not what will be measured during experiments and should hence only be viewed as a way of determining how well the edge states were localized. During the calculations, we have also seen a nonzero spin in the direction of the infinite lead which should not be the case as we have spin momentum locking. This was seen in Fig. 29. As this was a rather small density compared to the densities found for the other spins and the wave density itself, this can be attributed to a numerical artifact. However, we have also seen a spin precession along the surface states when considering those in the cones. These are large enough that they do not seem like numerical artifacts. If we consider that the spin is calculated over two layers and average over these layers, we find that the spin corresponds to the spin-momentum locking present.

7 Outlook

There are multiple ways to continue with the research on SnTe. One way is to improve the accuracy of the tight binding model by using an extended basis that also considers the s and d orbitals [40, 41]. This does however make the cost of calculating eigenvectors and eigenvalues far greater, which could prove to be a problem if the aim is to calculate wavefunctions with limited resources. However, this model has already been used in previous works where 2D systems were considered [42].

Another way to go is to focus on different surfaces. Experimentally the (100) surface is the most common for out-of-plane nanowires. However, when inplane growth is considered the (111) surface is more interesting. This surface is not as thoroughly discussed in the literature compared to the (100) surface. With this surface, you have a Dirac cone in the middle of the Brillouin zone and one at the edge. These do not hybridize but should give valid edge states if the surfaces and edges have the correct symmetries. Here it is recommended to start with a 2D model as the tight-binding matrix will be considerably smaller compared to the 3D model. This will allow the computation of the eigenvalues for greater thicknesses which are also experimentally relevant.

Experimentally it is also relevant to consider $Pb_xSn_{1-x}Te$, which acts as a TCI or an insulator depending on the value of x. Then one could question how the edge states would behave under different values of x. It would be expected that they still exist as long as $Pb_xSn_{1-x}Te$ is a TCI. However during the transition the surface states and hence the penetration depth change, which are both relevant to calculate.

Lastly for the tight binding calculations, one could determine the topological invariant with respect to one of the edge modes. This requires that the operator which is determined by the symmetries of the system is derived. This operator should give a different eigenvalue depending on the state of the edge mode. Then using this operator one can compute the existence of the edge modes without relying on visual cues.

References

[1] Liang Fu and C. L. Kane. Topological insulators with inversion symmetry. *Physical Review B*, 76(4):045302, July 2007. arXiv: cond-mat/0611341.

[2] A. Cook and M. Franz. Majorana fermions in a topological-insulator nanowire proximity-coupled to an s-wave superconductor. *Physical Review B*, 84(20):201105, November 2011.

[3] Liang Fu. Topological crystalline insulators. *Physical Review Letters*, 106(10):106802, March 2011. arXiv: 1010.1802.

[4] Timothy H. Hsieh, Hsin Lin, Junwei Liu, Wenhui Duan, Arun Bansil, and Liang Fu. Topological crystalline insulators in the SnTe material class. *Nature Communications*, 3(1):982, July 2012. arXiv: 1202.1003 Publisher: Nature Publishing Group.

[5] Yoichi Ando and Liang Fu. Topological Crystalline Insulators and Topological Superconductors: From Concepts to Materials. *Annual Review of Condensed Matter Physics*, 6(1):361–381, March 2015. arXiv: 1501.00531.

[6] Frank Schindler, Zhijun Wang, Maia G. Vergniory, Ashley M. Cook, Anil Murani, Shamashis Sengupta, Alik Yu. Kasumov, Richard Deblock, Sangjun Jeon, Ilya Drozdov, Hélène Bouchiat, Sophie Guéron, Ali Yazdani, B. Andrei Bernevig, and Titus Neupert. Higher-order topology in bismuth. *Nature Physics*, 14(9):918–924, September 2018. 578 citations (Crossref) [2024-03-07].

[7] Liang Fu and C. L. Kane. Superconducting proximity effect and majorana fermions at the surface of a topological insulator. *Physical Review Letters*, 100(9):096407, March 2008. arXiv: 0707.1692.

[8] Leena Aggarwal, Penghao Zhu, Taylor L. Hughes, and Vidya Madhavan. Evidence for higher order topology in Bi and Bi0.92Sb0.08. *Nature Communications*, 12(1):4420, July 2021.

[9] Avishek Adhikari and Mahima Ranjan Adhikari. *Basic Topology 1: Metric Spaces and General Topology*. Springer Nature Singapore, Singapore, 2022.

[10] Phys.org staff. When is a coffee mug a donut? topology explains it, October 2016. Accessed: 2024-12-08.

[11] Michael Hakl. *Magneto-optics of relativistic-like electrons in 3D solids*. PhD thesis, 12 2017.

[12] Joel E. Moore. The birth of topological insulators. *Nature*, 464(7286):194–198, March 2010. 2455 citations (Crossref) [2023-09-13].

[13] Topological Quantum Matter Group. Classification of topological insulators and superconductors, n.d. Accessed: 2024-12-08.

[14] Rami Ashour. Kramers theorem, n.d. Accessed: 2024-12-08.

[15] Kitinan Pongsangangan, T. Stoof, and Lars Fritz. Hydrodynamics of charged two-dimensional dirac systems i: thermo-electric transport, 06 2022.

[16] Yi Zhang, Ke He, Cui-Zu Chang, Can-Li Song, Li-Li Wang, Xi Chen, Jin-Feng Jia, Zhong Fang, Xi Dai, Wen-Yu Shan, Shun-Qing Shen, Qian Niu, Xiao-Liang Qi, Shou-Cheng Zhang, Xu-Cun Ma, and Qi-Kun Xue. Crossover of the three-dimensional topological insulator Bi2Se3 to the two-dimensional limit. *Nature Physics*, 6(8):584–588, August 2010. 1140 citations (Crossref) [2023-07-20].

[17] Y. Tanaka, Zhi Ren, T. Sato, K. Nakayama, S. Souma, T. Takahashi, Kouji Segawa, and Yoichi Ando. Experimental realization of a topological crystalline insulator in snte. *Nature Physics*, 8(11):800–803, September 2012.

[18] C. Ortix. Nonlinear hall effect with time-reversal symmetry: Theory and material realizations, 04 2021.

[19] Andrey Pravdivtsev, Danila Barskiy, Jan-Bernd Hövener, and Igor Koptyug. Symmetry constraints on spin order transfer in parahydrogen-induced polarization (phip). *Symmetry*, 14:530, 03 2022.

[20] Y. Tanaka, T. Sato, K. Nakayama, S. Souma, T. Takahashi, Zhi Ren, M. Novak, Kouji Segawa, and Yoichi Ando. Tunability of the k-space location of the dirac cones in the topological crystalline insulator $pb_{1-x}sn_x$te. *Phys. Rev. B*, 87:155105, Apr 2013.

[21] Junwei Liu, Wenhui Duan, and Liang Fu. Two types of surface states in topological crystalline insulators. *Physical Review B*, 88(24):241303, December 2013.

[22] Craig M. Polley, Ryszard Buczko, Alexander Forsman, Piotr Dziawa, Andrzej Szczerbakow, Rafał Rechciński, Bogdan J. Kowalski, Tomasz Story, Małgorzata Trzyna, Marco Bianchi, Antonija Grubišić Čabo, Philip Hofmann, Oscar Tjernberg, and Thiagarajan Balasubramanian. Fragility of the dirac cone splitting in topological crystalline insulator heterostructures. *ACS Nano*, 12(1):617–626, December 2017.

[23] Nguyen Minh Nguyen, Wojciech Brzezicki, and Timo Hyart. Corner states, hinge states and Majorana modes in SnTe nanowires. *Physical Review B*, 105(7):075310, February 2022. arXiv: 2105.11489.

[24] Chao-Xing Liu, Xiao-Liang Qi, HaiJun Zhang, Xi Dai, Zhong Fang, and Shou-Cheng Zhang. Model Hamiltonian for topological insulators. *Physical Review B*, 82(4):045122, July 2010. arXiv: 1005.1682.

[25] Mahmoud M. Asmar, Daniel E. Sheehy, and Ilya Vekhter. Topological phases of topological-insulator thin films. *Physical Review B*, 97(7):075419, February 2018. arXiv: 1801.02084 Publisher: American Physical Society.

[26] Junwei Liu, Timothy H. Hsieh, Peng Wei, Wenhui Duan, Jagadeesh Moodera, and Liang Fu. Spin-filtered edge states with an electrically tunable gap in a two-dimensional topological crystalline insulator. *Nature Materials*, 13(2):178–183, February 2014. arXiv: 1310.1044.

[27] D L Mitchell, R F Wailis, F Seitz, D Turnbull, J F Butler, A R Calawa, R J Phelan, T C Harman, A JStrauss, R H Rediker, D G Sell, D M Hum, L Pincherle, D W Sciama, P M Woodward, Proc A Roy Soc, J BConklin, L E Johnson, G W Pratt, P J Lin, L Kleinman, Phys Rev, J B Conklin, E Pikus, G L Bir, G E Pikus, Ed Palik, JN Zemel, DL Mitchell, E D Palik, J N Zemel, K F Cuff, M R Ellett, C D Kuglin, and L R Williams. English transl. :Soviet Phys.-Solid State. Technical report, Academic Press Inc, 1959. Publication Title: Proc. Phys. Soc. (London) Volume: 9.

[28] Dániel Varjas, Tómas Ö Rosdahl, and Anton R Akhmerov. Qsymm: Algorithmic symmetry finding and symmetric Hamiltonian generation. *New Journal of Physics*, 20(9):093026, September 2018. 23 citations (Crossref) [2023-09-13] arXiv:1806.08363 [cond-mat].

[29] Robert G. Littlejohn. Lecture notes on hilbert space, physics 221, fall 2020. `http://bohr.physics.berkeley.edu/classes/221/1112/notes/hilbert.pdf`, 2020. Accessed: 2024-12-08.

[30] Mahmoud M. Asmar, Daniel E. Sheehy, and Ilya Vekhter. Interface symmetry and spin control in topological-insulator-semiconductor heterostructures. *Physical Review B*, 95(24):241115, June 2017. arXiv: 1611.06110 Publisher: American Physical Society.

[31] Alexander Lau and Carmine Ortix. Topological Semimetals in the SnTe Material Class: Nodal Lines and Weyl Points. *Physical Review Letters*, 122(18):186801, May 2019. arXiv: 1804.09574 Publisher: American Physical Society.

[32] J. Kiefer. Sequential minimax search for a maximum. *Proceedings of the American Mathematical Society*, 4(3):502–506, June 1953.

[33] Christoph W Groth, Michael Wimmer, Anton R Akhmerov, and Xavier Waintal. Kwant: a software package for quantum transport. *New Journal of Physics*, 16(6):063065, June 2014. 769 citations (Crossref) [2023-10-06].

[34] Detlef Rorink. Topology in lead tin telluride: A theoretical study of hybridized surface states. Master's thesis, University of Twente, 2024.

[35] Sohrab Rabii. Energy-band structure and electronic properties of snte. *Phys. Rev.*, 182:821–828, Jun 1969.

[36] Hideyuki Ozawa, Ai Yamakage, Masatoshi Sato, and Yukio Tanaka. Topological phase transition in a topological crystalline insulator induced by finite-size effects. *Physical Review B*, 90(4):045309, July 2014. Publisher: American Physical Society.

[37] Yung Jui Wang, Wei-Feng Tsai, Hsin Lin, Su-Yang Xu, M. Neupane, M. Z. Hasan, and A. Bansil. Nontrivial spin texture of the coaxial Dirac cones on the surface of topological crystalline insulator SnTe. *Physical Review B*, 87(23):235317, June 2013. arXiv: 1304.8119.

[38] Roni Majlin Skiff, Fernando de Juan, Raquel Queiroz, Haim Beidenkopf, and Roni Ilan. Confined vs. extended Dirac surface states in topological crystalline insulator nanowires. *ArXiv.org*, September 2021. arXiv: 2109.02023.

[39] Junwei Liu and Liang Fu. Electrically tunable quantum spin Hall state in topological crystalline insulator thin films. *Physical Review B*, 91(8):081407, February 2015. arXiv: 1501.05632 Publisher: American Physical Society.

[40] Lent. Relativistic empirical tight-binding theory of the energy bands of gete, snte, pbte, pbse, pbs, and their alloys. 1986.

[41] MT P.S. Keizer, Wimmer, D Varjas, and H Spring. Band structure calculations of the topological crystalline insulator SnTe. Technical report, Eindhoven University of Technology, 2021.

[42] Max Hoskam, E P A M Bakkers, P Leubner, R Op Het Veld, M Wimmer, and D Varjas. Theory and Fabrication of SnTe for Majorana devices. Technical report, Eindhoven University of Technology, 2018.

A Appendix A

Here the logarithmic plot of the SnTe wave function is given for the adjusted Hsieh Hamiltonian given in equation 4. Fig. 26 shows a clear linear relationship from which the penetration depth can be determined. This results in a value of 3.4 nm.
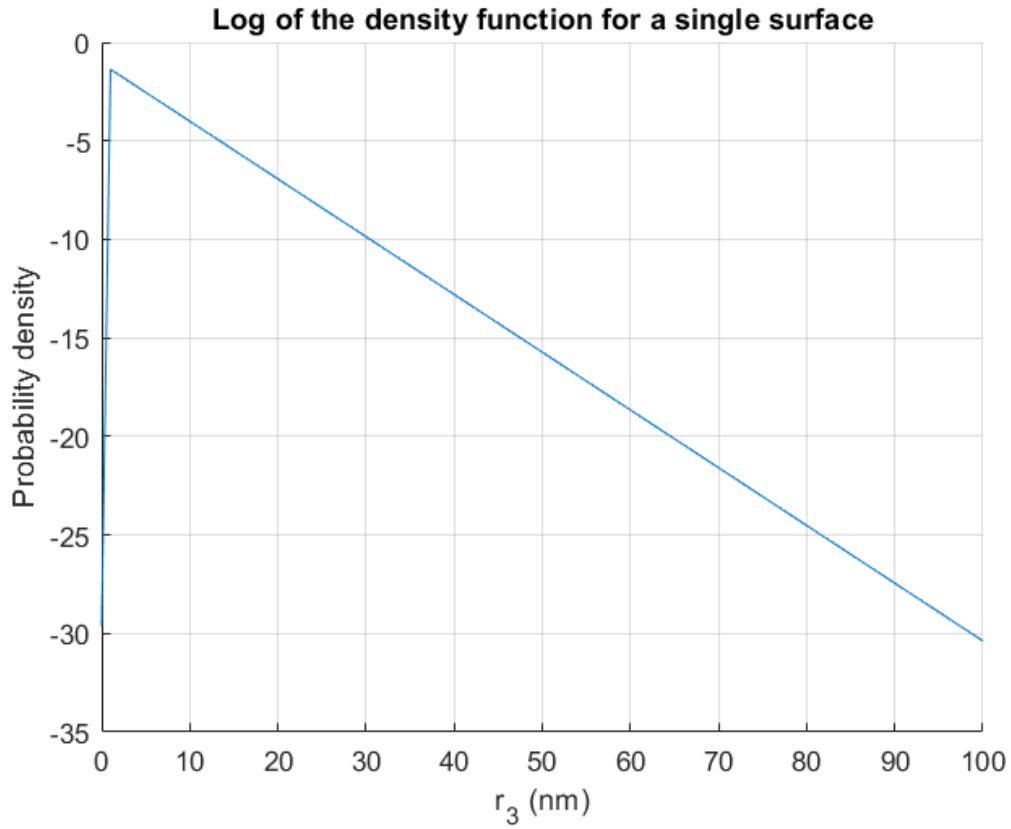

FIGURE 26: The same figure as Fig. 8 however now with the natural logarithm on the y-axis. This shows a clear linear correlation showing that the Density is an exponential function.

B Appendix B

In this appendix, figures can be found that show spin and wave density behavior for specific configurations of the nanowire in the tight-binding model. They are referred to and addressed in section 4.
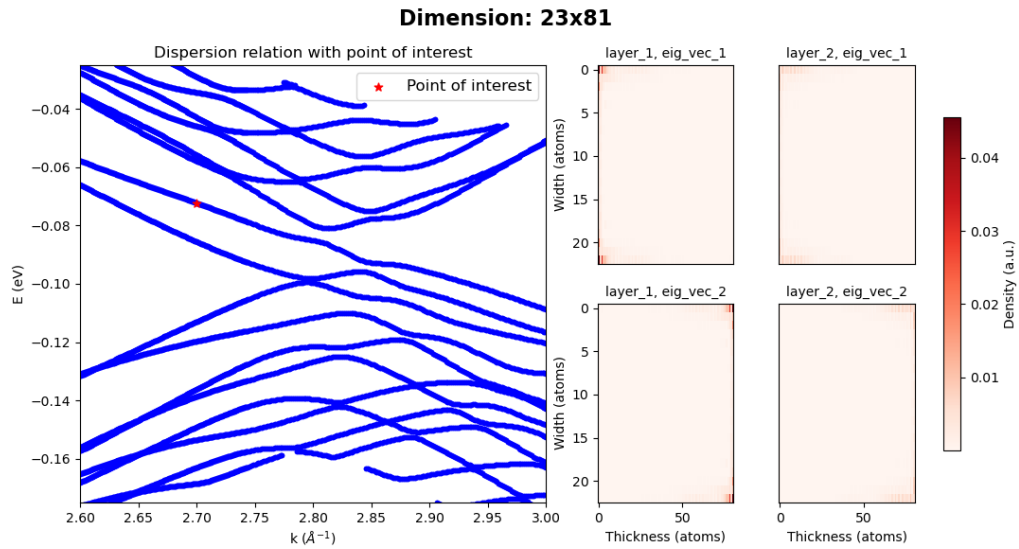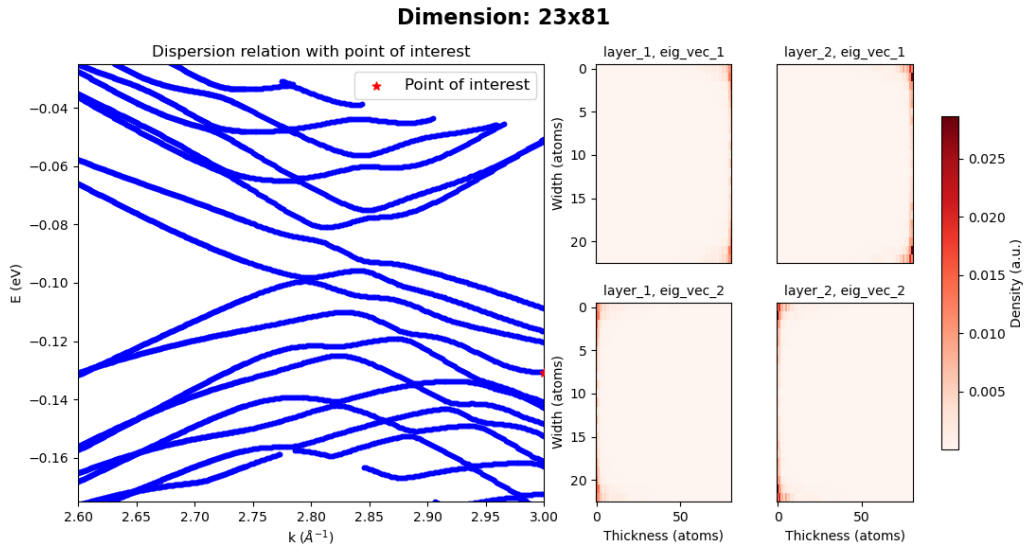

FIGURE 27: Dispersion relation (left) and the corresponding wave functions in real space (right). Each wave function corresponds to a layer and degeneracy pair. The probability density considered is at the highest edge state for k=2.7.

FIGURE 28: Dispersion relation (left) and the corresponding wave functions in real space (right). Each wave function corresponds to a layer and degeneracy pair. The probability density considered is at the lowest edge state for k=3.0.
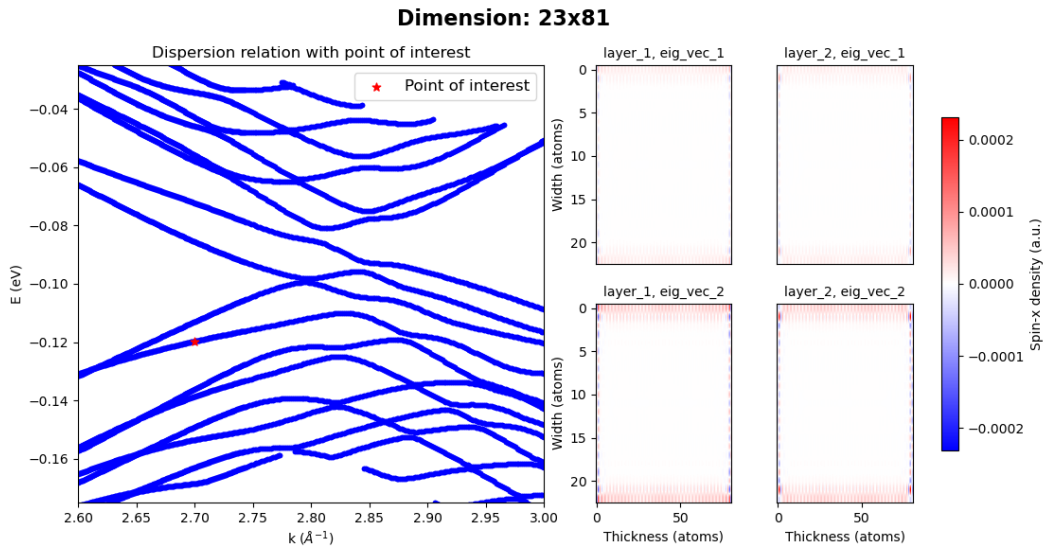

FIGURE 29: Dispersion relation (left) and the corresponding spin density in the x direction in real space (right).
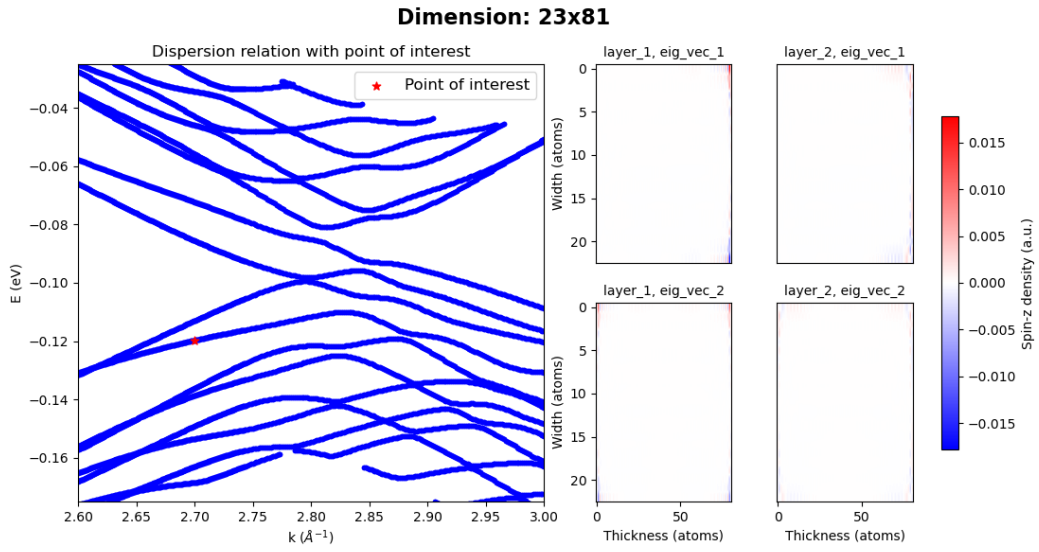
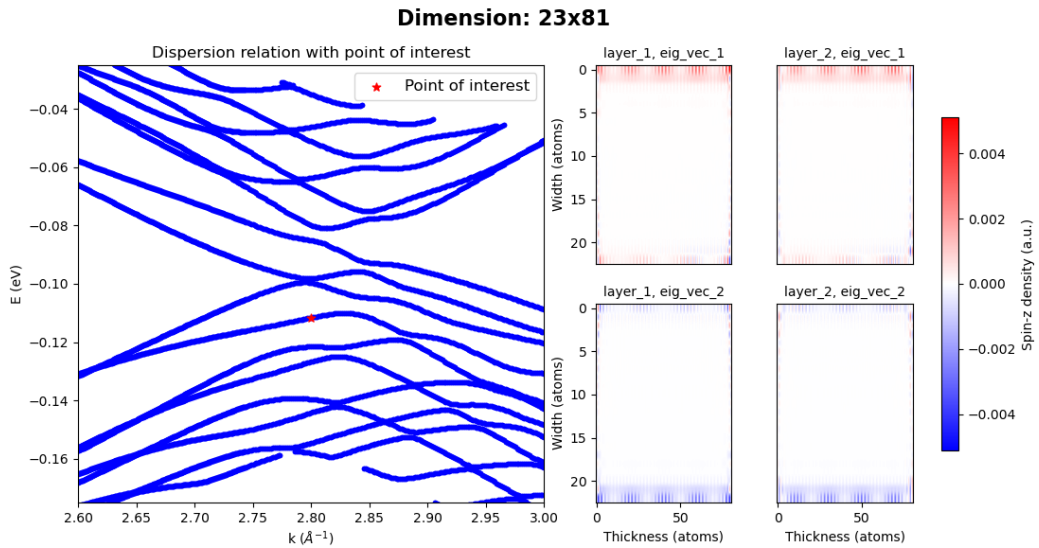FIGURE 30: Dispersion relation (left) and the corresponding spin density in the z direction in real space (right).

FIGURE 31: Dispersion relation (left) and the corresponding spin density in the z direction in real space (right). The point of interest in chosen such that the wave function is in between the tops of the Dirac cone.